Summer 7-10-2024

GNSS and InSAR Observations of Vertical Motion in the Valles Caldera, NM

Savannah Chase Devine

Savannah C. Devine

Candidate

Earth and Planetary Sciences

Department

This thesis is approved, and it is acceptable in quality and form for publication:

Approved by the Thesis Committee:

Eric Lindsey, Chairperson

Mousumi Roy

Brandon Schmandt

GNSS and InSAR Observations of Vertical Motion in the Valles Caldera, NM

By

Savannah C. Devine

B.S. GEOLOGY, APPALACHIAN STATE UNIVERSITY, 2022

THESIS

Submitted in Partial Fulfillment of the Requirements for the Degree of

Master of Science

Earth and Planetary Science

The University of New Mexico

Albuquerque, New Mexico

July 2024

ACKNOWLEDGEMENTS

This work would not be possible without the help of the members of my committee (Eric Lindsey, Brandon Schmandt, Mousumi Roy), as well as the co-authors of the GPS portion of this project (Nathan Maier, Ronni Gropenthin, Andy Newman).

GNSS and InSAR Observations of Vertical Motion in the Valles Caldera, NM

By

Savannah C. Devine

B.S., Geology, Appalachian State University, 2022

M.S., Earth and Planetary Sciences, University of New Mexico, 2024

ABSTRACT

The Valles caldera is a rhyolitic “supervolcano” formed 1.231 Ma. An understanding of whether Valles caldera is currently deforming is needed to inform volcanic hazard estimates for northern New Mexico and will allow for a better understanding of the hazards presented by other rhyolitic caldera systems. Here, we present an InSAR time series of the Valles Caldera using 37 interferograms, spanning 2014 to 2022, which show a small but consistent signal of broad pattern subsidence <1 mm/yr. We also present GNSS observations from a survey conducted in October 2022 and compare the results to surveys in 2002 and 2003 to estimate the cumulative deformation, showing an average vertical movement of <2 mm/yr. The GPS results are modeled using the deformation model from Mogi (1958) and show a best-fitting depth of 12 km. Within Valles, installation of a continuous GPS network would reveal and help isolate seasonal and long-term deformation.

TABLE OF CONTENTS

ABSTRACT……...iv

TABLE OF CONTENTS…….……..…v

LIST OF FIGURES…..……..…vii

LIST OF TABLES…….…….…….x

1. INTRODUCTION…….…….…….....…..…1

1.1 Geologic Setting…….……..…..….1

1.2 Recent Activity…….……...……...…3

1.3 Use of InSAR…….……..……..6

1.4 Use of GNSS…….…….……8

1.5 Long Valley Caldera…….…….8

1.6 Deformation Modeling…….……..9

2. METHODS & RESULTS…….…….……10

2.1 InSAR Processing using ISCE…….…...….11

2.2 Creating Approximately year-long interferograms……..……..……..14

2.3 GNSS Processing……..……..…..17

2.4 Mogi model results…….……..……30

3. DISCUSSION…….……39

3.2 Fluid Migration……..…….……..39

3.3 Magma crystallization……..……40

3.4 Regional subsidence…….……41

3.5 changes in rainwater mass……..……..43

4. CONCLUSIONS……...…….43

5. REFERENCES……...45

6. APPENDICIES

LIST OF APPENDICIES……..……51

APPENDIX 1……52

LIST OF FIGURES

Figure 1……..2

Figure 2……..3

Figure 3……..5

Figure 4……..6

Figure 5……10

Figure 6……12

Figure 7……13

Figure 8……14

Figure 9……15

Figure 10……..……16

Figure 11……..……19

Figure 12……..……21

Figure 13……..……22

Figure 14……..……23

Figure 15……..……25

Figure 16……..……26

Figure 17……..……26

Figure 18……..……27

Figure 19……..……28

Figure 20……..……29

Figure 21……..……30

Figure 22……..……32

Figure 23……..……33

Figure 24……..…….34

Figure 25……..…….35

Figure 26……..…….35

Figure 27……..…….37

Figure 28……..…….38

Figure 29……..…….39

Figure 30……..…….42

Figure A1……..52

Figure A2……..53

Figure A3……..54

Figure A4……..55

Figure A5……..56

Figure A6……..57

Figure A7……..58

Figure A8……..59

Figure A9……..60

Figure A10..……..61

Figure A11..……..62

Figure A12..……..63

Figure A13..……..64

Figure A14..……..65

Figure A15..……..66

Figure A16..……..67

Figure A17..……..68

Figure A18..……..69

Figure A19..……..70

Figure A20..……..71

Figure A21..……..72

Figure A22..……..73

Figure A23..……..74

Figure A24..……..75

LIST OF TABLES

Table 1...……..…….17

Table 2...……..…….33

1. INTRODUCTION

1.1 Geologic Setting

The Valles caldera complex **(**Figure 1**)** is a large rhyolitic caldera system, as are the Yellowstone and Long Valley caldera systems (Vasco et al., 2007; Tizzani et al., 2007). Rhyolitic volcanoes (which are commonly associated with ring fractures and resurgent domes) pose a potential hazard to population regions (Figure 2). While basaltic eruptions are typically effusive and flow more as a liquid, rhyolitic eruptions can be explosive in some cases, although effusive rhyolitic eruptions can occur (for example, the rhyolite domes in Valles formed from effusive eruptions). Explosive eruptions form large volumes of lava as well as pumice and ash; this is because they are more viscous and typically build up a significant amount of ash prior to eruption.

The Valles caldera is part of the Jemez Mountains volcanic field, which has been geologically active for >15 million years (Wolff et al., 2011; Kelley et al., 2013). A caldera-forming eruption at 1.62 ±0.04 Ma led to the creation of the Toledo caldera (Spell et al., 1996), which was then followed by Valles at 1.231 ± 0.001 Ma (Nasholds and Zimmerer, 2022). The caldera complex likely formed due to extensional forces at the intersection of the Rio Grande rift (~30 Ma) and the Jemez Lineament (Wannamaker, 1997; Goff and Kelley, 2021), and long-term rise of basaltic to rhyolitic magmas (Kelley et al., 2013).

Between 1.23 – 0.52 Ma, multiple eruptions around the Valles ring fracture zone caused the formation of rhyolitic (high in silica) lava domes and minor tuffs in the caldera (Goff et al., 2011). This was followed by a dormant period of around 460 ka, which ended in the last intracaldera eruption at 68.3 ±1.5 ka (Zimmerer et al., 2016; Nasholds and Zimmerer, 2022).

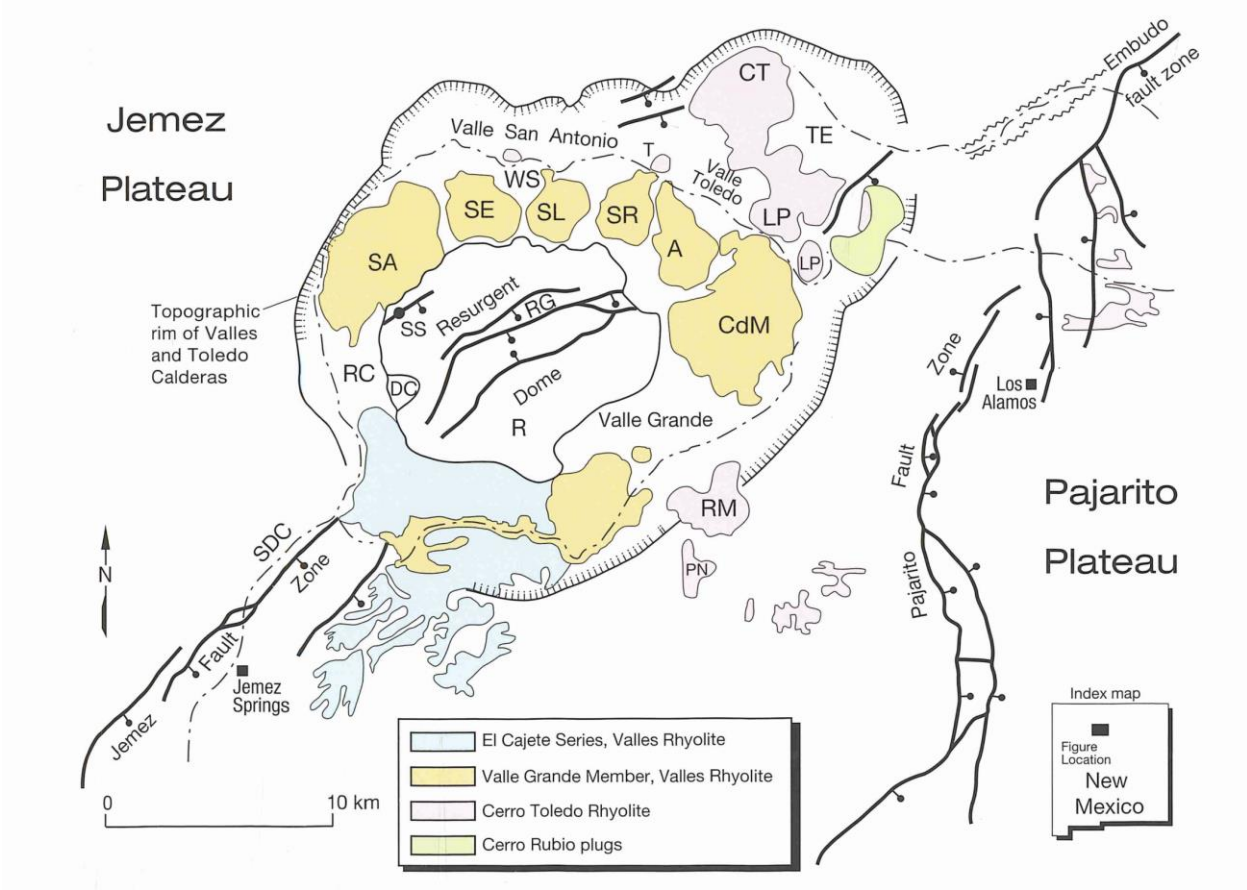

Figure 1. A map of the Jemez region in Northern New Mexico, within the Jemez Plateau (Goff, 2009). The major units are indicated in the key, including the Ek Cajete series, the Valle Grande Member, the Cerro Toledo Rhyolite, and the Cerro Rubio plugs. The lava domes (Valle Grande Member) were formed during the period of activity between 1.23-0.52 million years ago (Goff et al., 2011).

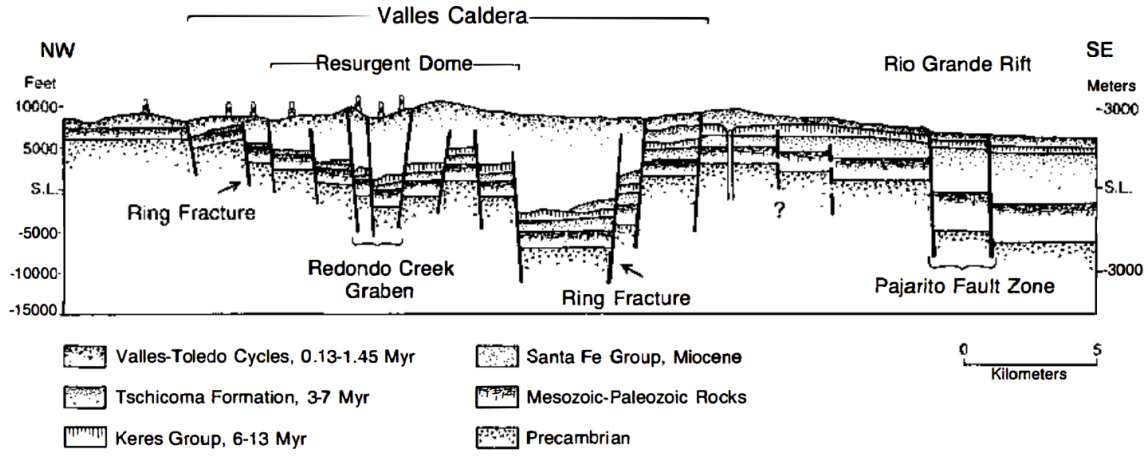

Figure 2. A cross sectional diagram of the Valles caldera, indicating the resurgent dome, ring fracture, and Pajarito Fault Zone (Heiken et al., 1990). Ring fractures are common in caldera complexes, and form alongside the caldera itself.

1.2 Recent Activity

The youngest eruption at 68.3 ±1.5 ka was preceded by the El Cajete Pyroclastic Beds and the Battleship Rock Ignimbrite at 74.4 ±1.3 ka (Goff et al, 2011; Wolff et al., 2011; Zimmerer et al., 2016). Wolff and Gardner (1995) argue that the Valles caldera may be entering a new cycle of activity because of mafic magma intrusion in the southern ring fracture zone.

A better understanding of the current deformation (and potential volcanic activity) of this caldera complex and its potential to reactivate would allow for a more accurate volcanic risk and hazard assessment in the area. This also applies to other regions that may be impacted by similar systems, including the Yellowstone and Long Valley calderas in the US, and other rhyolitic calderas worldwide, such as Rabaul in Indonesia (Garthwaite et al., 2019). Geodetic observations across the US Southwest indicate a broad pattern of subsidence at rates less than 1 mm/yr within the Rio Grande rift and part of the Jemez Lineament (Murray et al., 2019, Berglund et al., 2012).

This may be related to active tectonic deformation within this region and should be considered when observing a more localized deformation source within this area.

Faults in the region typically slip at rates less than 0.2 mm/yr (van Wijk et al., 2018). It is hypothesized that the measurable observed deformation is a direct result of ongoing rifting, and not related to some other source of deformation within the caldera (Murray et al., 2019, Berglund et al., 2012).

Seismic studies dating back to 1981 indicate the presence of a low velocity zone, which implies the presence of partially liquid magma (Suhr, 1981; Roberts et al., 1991). The most recent studies have constrained this low velocity zone to 3-10 km below Redondo Peak (Figure 3) (Wilgus et al., 2023). Wilgus and others (2023) estimate an approximate volume of 40 km^3 and a melt fraction of ~20% for the magma body. Geodetic data used alongside seismic studies can provide the location of the magma body as well as any surface deformation it may be causing (Figure 4).

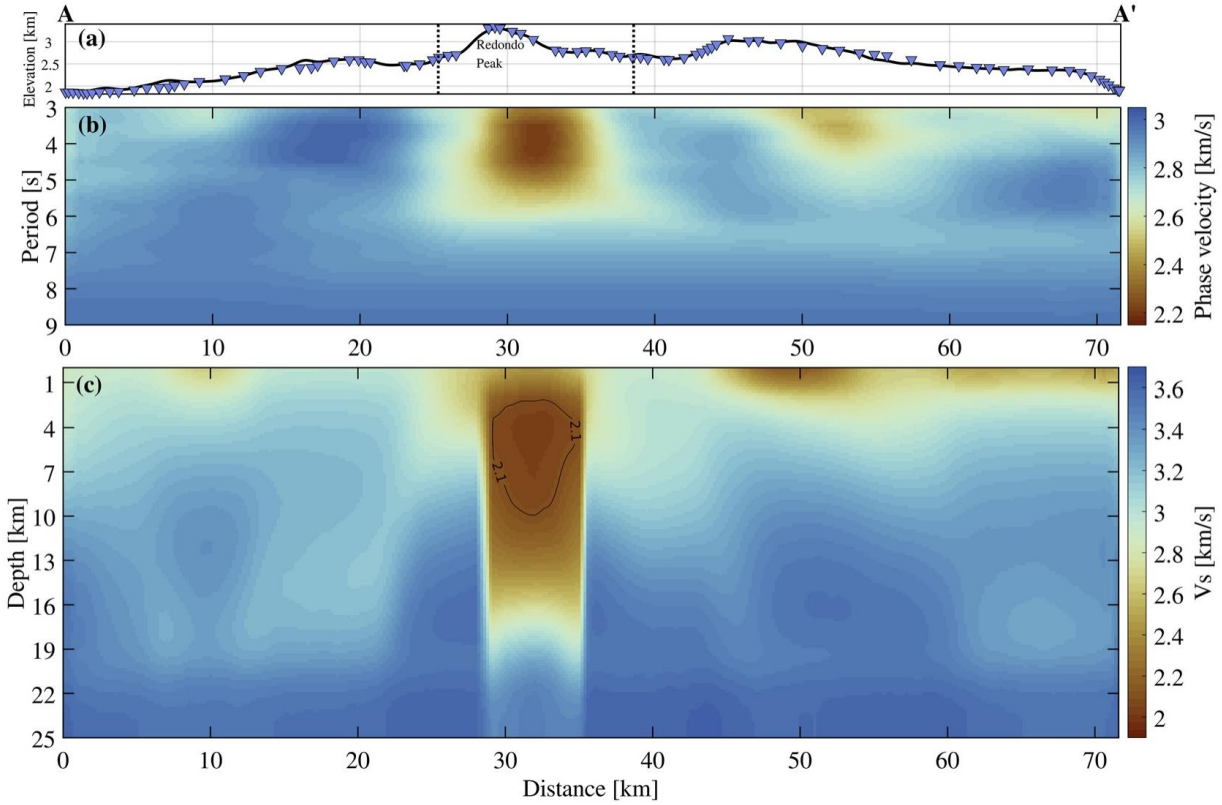

Figure 3. Tomographic cross section of the Valles caldera from Wilgus et al. (2023) that runs southwest to northeast. This shows a low velocity zone underneath Redondo Peak which indicates a partially molten magma body. There appears to be other regions with lower velocities in comparison to the surrounding rock, but the zone beneath Redondo Peak is the most prominent and goes the deepest.

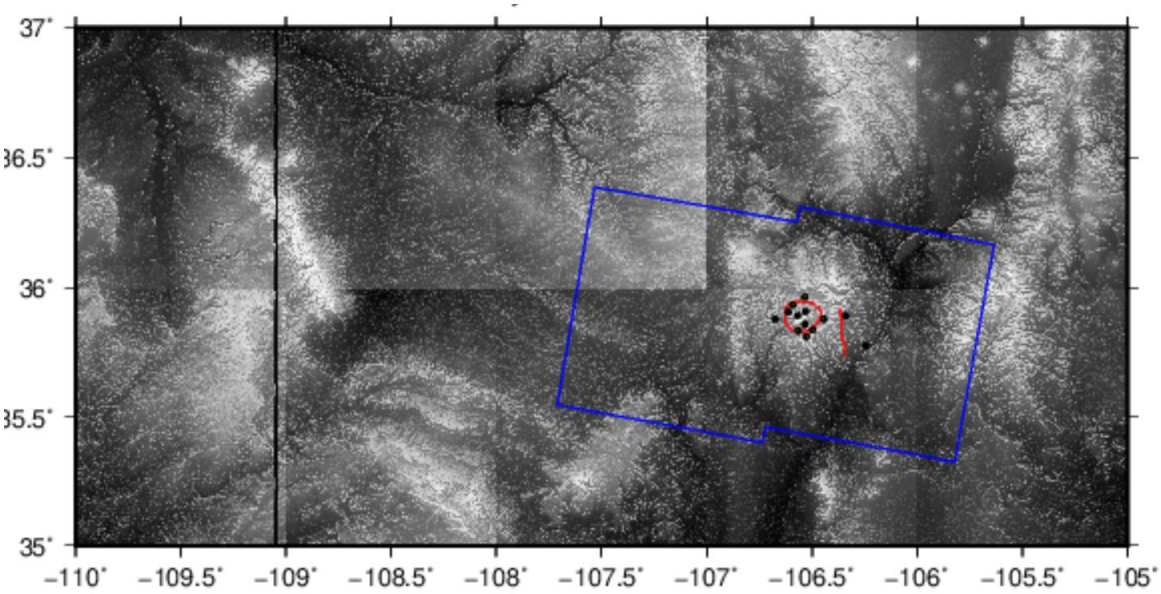

Figure 4. A map of the general Valles caldera region. The area that we processed using InSAR is indicated here in blue, the ring fracture and Pajarito Fault are indicated in red, and the GPS stations are indicated by black dots.

1.3 Use of InSAR

Interferometric synthetic aperture radar (InSAR) is commonly used to measure ground deformation over wide areas and can detect movement over timescales of weeks to years. SAR (synthetic aperture radar) is an active remote sensing method that uses microwaves to image objects and surfaces (Bamler and Hartl, 1998). InSAR is a method of analyzing SAR imagery by determining the phase differences between two or more SAR images taken from different positions or times to measure topography or deformation, respectively (Bamler and Hartl, 1998). Our study uses data from Sentinel-1 (1-A and 1-B), a European Space Agency satellite mission that collects SAR images every 12 days over much of the world. The effectiveness of InSAR for studying deformation varies due to noise from vegetation, the troposphere, and the ionosphere

(Treuhaft et al., 1996; Bekaert et al., 2015; Liang et al., 2019). These errors can contribute to lower accuracy as compared to Global Navigation Satellite Systems (GNSS). Moreover, the estimated horizontal motion has lower accuracy due to the "look angle" of the satellite being nearly vertical (Wright et al., 2004).

InSAR has been used to observe volcanic deformation since around 1995, with initial application to Mount Etna in Italy (Massonnet et al., 1995). This method allows for volcano deformation to be mapped across a much larger area and at relatively longer time scales (depending on the mission lifetime of the satellite used) as compared to other techniques, and can be used in places where ground monitoring was previously sparse or is too dangerous, which is frequently the case for volcanoes. InSAR was soon applied on a much larger scale with application to both volcanic signals and other types of ground deformation, such as fault-related deformation or groundwater motion (Poland and Zebker, 2022). Fialko and Simons (2001) use InSAR to estimate deformation due to the Socorro Magma body, which is another volcanic system in the central Rio Grande rift, New Mexico, that remains active to date (Block et al., 2023).

InSAR has previously been used to observe crustal deformation in Yellowstone, a caldera complex similar to Valles caldera, resulting in a detailed map of subsidence in the region (Dzurisin et al., 1990). By imaging the long-term surface deformation of a region with high spatial resolution, we can better understand the location and depth of the subsurface sources of the motion, significantly improving our hazard modeling of that caldera system. In this study, we used InSAR to estimate the deformation pattern within the Valles caldera over time scales of months to years.

1.4 Use of GNSS

The Global Navigation Satellite Systems (GNSS), which includes the US-based Global Positioning System (GPS), allows for precise measurement of changes in site positions over timescales of seconds to decades at specific sites (Bock et al., 2000). In the case of volcanic deformation, GNSS sites are typically used to observe both horizontal and vertical deformation at multiple sites throughout an active region, with greater accuracy and higher temporal resolution than InSAR, but at a much lower spatial density (e.g. Palano et al., 2023).

Continuous GNSS sites measure ground deformation at permanent observing stations without interruption over long time scales. In contrast, survey-mode observations can be made using temporary GNSS stations installed for several days at multiple nearby benchmarks in the same area. This allows for spatially denser data. GNSS was not initially created for scientific purposes but has since become the foundation of modern geodesy. This is thanks to its millimeter-level precision and accuracy (Perosanz, 2019). Here, we use survey GNSS observations to measure long-term deformation in the Valles Caldera on decadal time scales.

1.5 Long Valley Caldera

The Long Valley caldera is 17 by 32 km in the Sierra Nevada region, with several resurgent domes that formed ~0.7 million years ago (Bailey et al., 1976). Geodetic studies indicate a consistent uplift that has spanned several decades (Langbein, 2003; Webb et al., 1995; Silverii et al., 2021). Based on both geodetic and seismic data, this uplift is a direct result of inflation of an underlying magma body (Silverii et al., 2021). As a result, the Long Valley caldera system is considered to be active, and continues to be studied and monitored for potential changes due to its proximity to populated regions.

The continuous monitoring of the Long Valley caldera has allowed for multiple models to be published of the deformation source within the region (Battaglia et al., 2003). Beginning in January 1993, with the installation of the first continuous GPS monument (CASA) (Dixon et al., 1997), this region has been continuously monitored in order to observe its deformation and in case of any potential changes.

1.6 Deformation Modeling

The Mogi (1958) model shows the inflation or deflation of a point source or sphere in an elastic half-space. This is commonly used to model volcanic deformation, where the source represents a magmatic body, often using geodetic data. The results show deformation at the surface, both horizontal and vertical. For the point source model, the required parameters are radial distance from the source, depth to the center of the source, volumetric change of the sphere, and poisson's ratio. This is commonly used with geodetic data such as InSAR and GNSS to model magmatic sources within volcanoes (Saltogianni and Stiros, 2013).

Using the method from Mogi (1958), this form of deformation modeling assumes that the medium that the source is in is fully elastic, homogeneous, and has perfectly flat topography; it also assumes that the source is a point or perfectly spherical (Taylor et al., 2021) (Figure 5). As a result, this is far from a perfect method to model the often complex geometry of sources and varying rheologic properties of the surrounding bedrock in volcanic regions. However, it allows for a simple way to estimate the general location and volume or pressure change in magmatic or hydrothermal deformation sources. The "penny-shaped crack" model is similar to the Mogi technique, but it is usually more representative of a sill, where the source is not spherical or a

point source (Wang and Li, 2004). This model makes similar assumptions to the Mogi method, but allows for slightly more realistic geometry in certain cases.

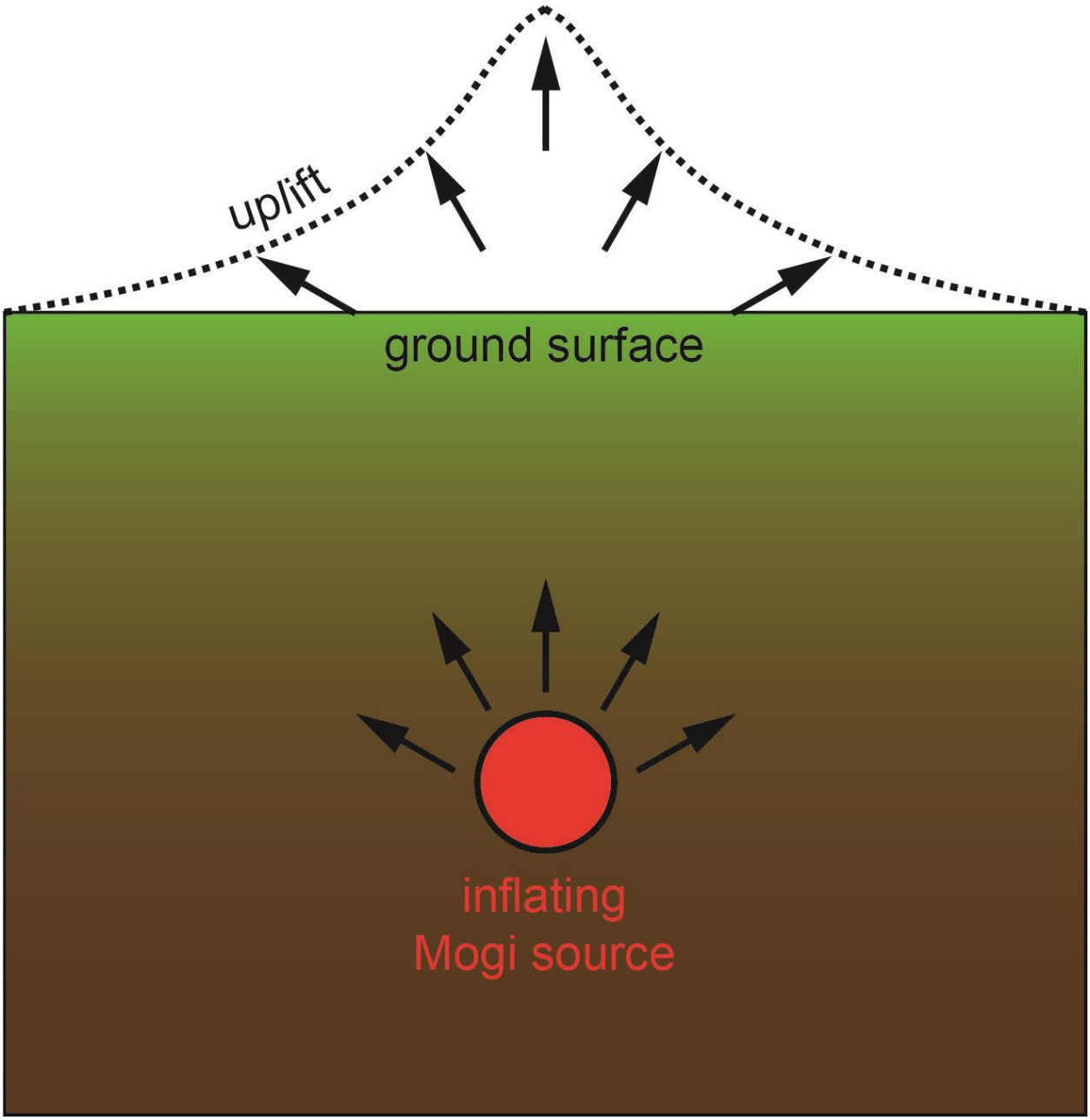

Figure 5. A schematic of the Mogi (1958) model (Poland, 2020).

2. METHODS & RESULTS:

2.1 InSAR Processing using ISCE

We processed Sentinel-1A data for this region using the open-source InSAR Scientific Computing Environment (ISCE) version 2 (Rosen et al., 2012) on a high-performance computing system maintained by the University of New Mexico Center for Advanced Research Computing (CARC).

We downloaded 410 Sentinel-1A scenes covering the Valles caldera from descending path number 56 from the Alaska Satellite Facility (https://search.asf.alaska.edu/#/). A digital elevation model (DEM) from the SRTM-GL1 dataset (Jain et al., 2018), referenced to the WGS84 ellipsoid, was used to remove topographic (parallax) effects from the interferometry. We selected 37 interferograms spanning the time period 2014-2022, after an initial processing of 188 interferograms. These interferograms had high spatial coherence, meaning there was little noise and the data was useful in finding signals of deformation and final velocities in the time series.

Additional processing steps included using the Goldstein Filter, which utilizes a Fourier Transform of the interferogram patch by patch to separate primary signals from noise, with a filter strength of 0.5. We used 3 azimuth and 5 range looks (down sampling) to improve coherence and reduce speckle noise (which is related to the roughness of the surface), and set the coherence threshold (which determines how similar a pixel is in different SAR observations) at 0.7. The ISCE software creates and executes a series of scripts to process the stack of images, by first identifying where the images overlap, extracting a valid region and aligning the images precisely, computing and filtering the interferograms and correcting them for topography, merging the separate subswaths (a series of bursts, which are images taken by the satellite) into

one image, and then unwrapping the final interferograms using the Snaphu algorithm (Chen and Zebker, 2001).

Two of the final interferograms (May 2, 2017 to May 14, 2017, and May 28, 2019 to May 22, 2020) are shown in Figures. 6 and 7, with phase shown in color and amplitude shown as pixel brightness. The pattern of phase variation in these images reflect mostly atmospheric noise due to humidity, temperature, and pressure changes between the two SAR acquisition dates, and were accounted for in the later time series analysis. Once we go through the quality of each interferogram, we used Mintpy to create the time series (Yunjun et al., 2019).

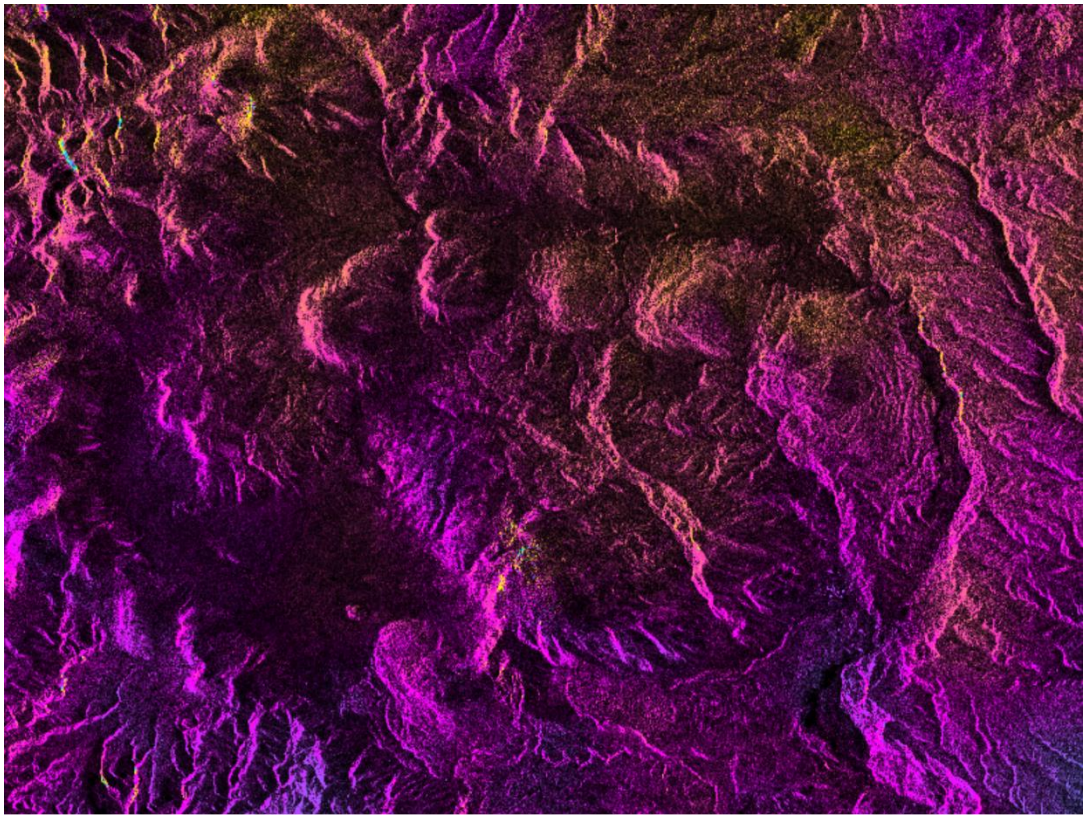

Figure 6. The interferogram of the Valles caldera created using ISCE version 2 for May 2, 2017 to May 14, 2017. One phase cycle in the image is equal to 2.3 cm, and the brightness of the

pixels reflect the radar reflection amplitude. In this image, there is very little deformation, which is why the majority of the image is the same color.

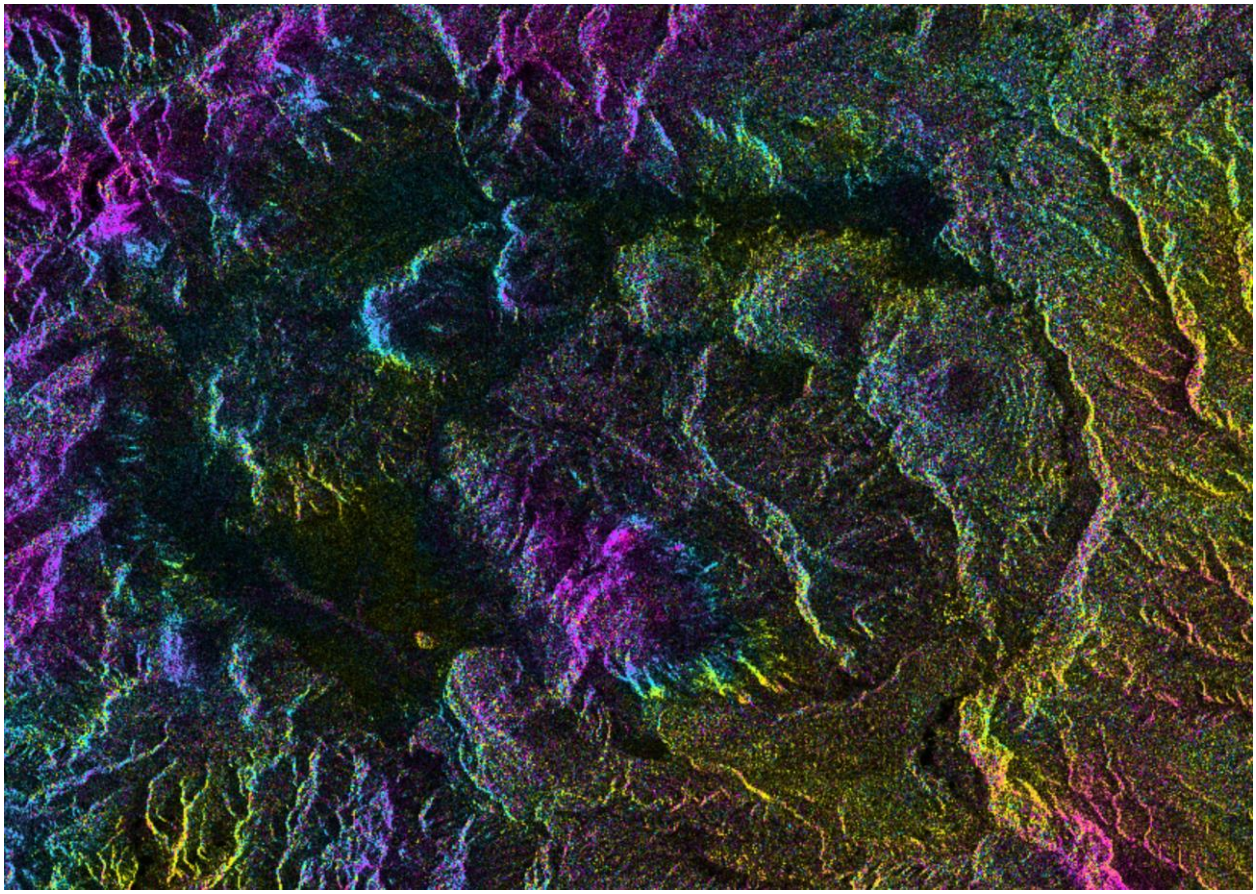

Figure 7. The interferogram of the Valles caldera created using ISCE version 2 for May 28, 2019 to May 22, 2020. One phase cycle in the image is equal to 2.3 cm, and the brightness of the pixels reflect the radar reflection amplitude. Much of the color change visible in this figure is due to noise from topographically correlated water vapor delays, not real deformation, which can be common in individual interferograms. In the final velocity map, these effects are reduced by averaging many images together.

2.2 Creating Approximately year-long interferograms

To decrease noise levels due to low phase coherence in some images (Figure 8), we used primarily year-long interferograms and did not process data collected during winter months, because snow absorbs most of the radar signal (Figure 9). We chose interferograms between the months of May and June because these are the time periods least likely to have high amounts of noise due to snowpack or humidity.

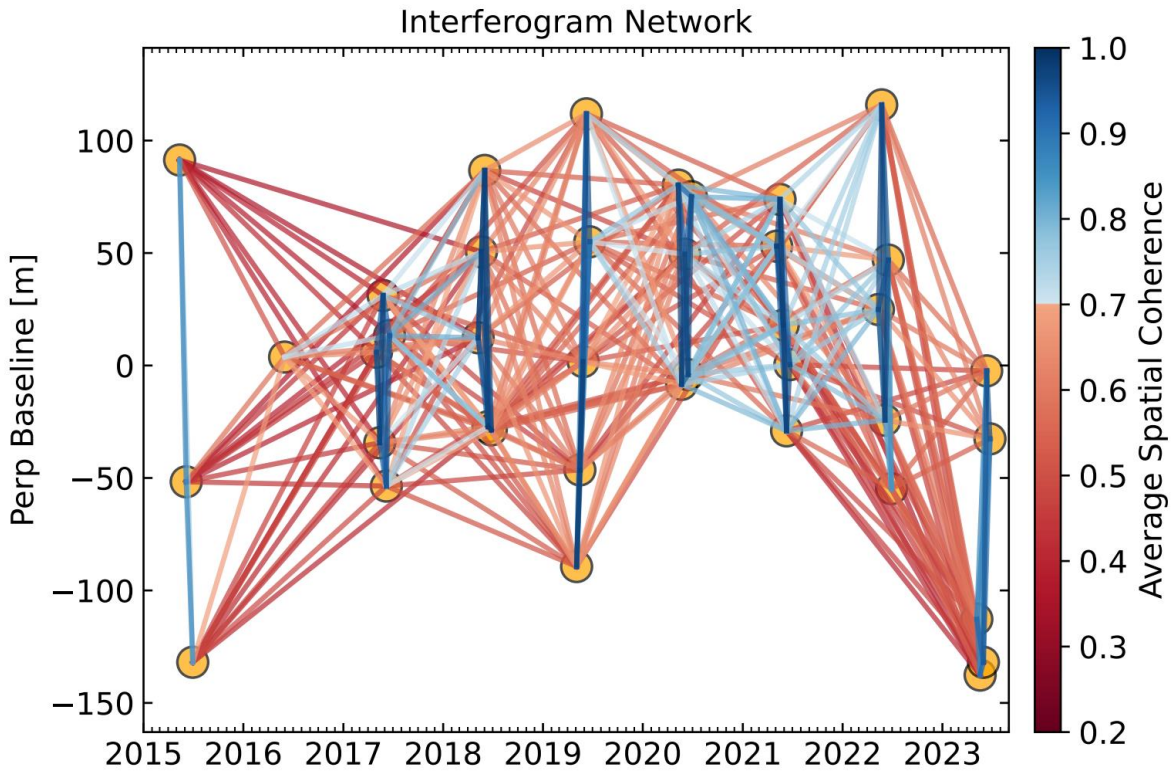

Figure 8. A set of interferograms from the initial Valles processing. The x-axis is time in years, and the y-axis is perpendicular baseline. The lines represent individual interferograms. The dots are SAR acquisitions, and the red lines are interferograms where the majority of the data was unusable due to the spatial coherence being too low, while the blue lines represent interferograms with mostly usable data. The majority of these are red, meaning the majority of interferograms were low coherence.

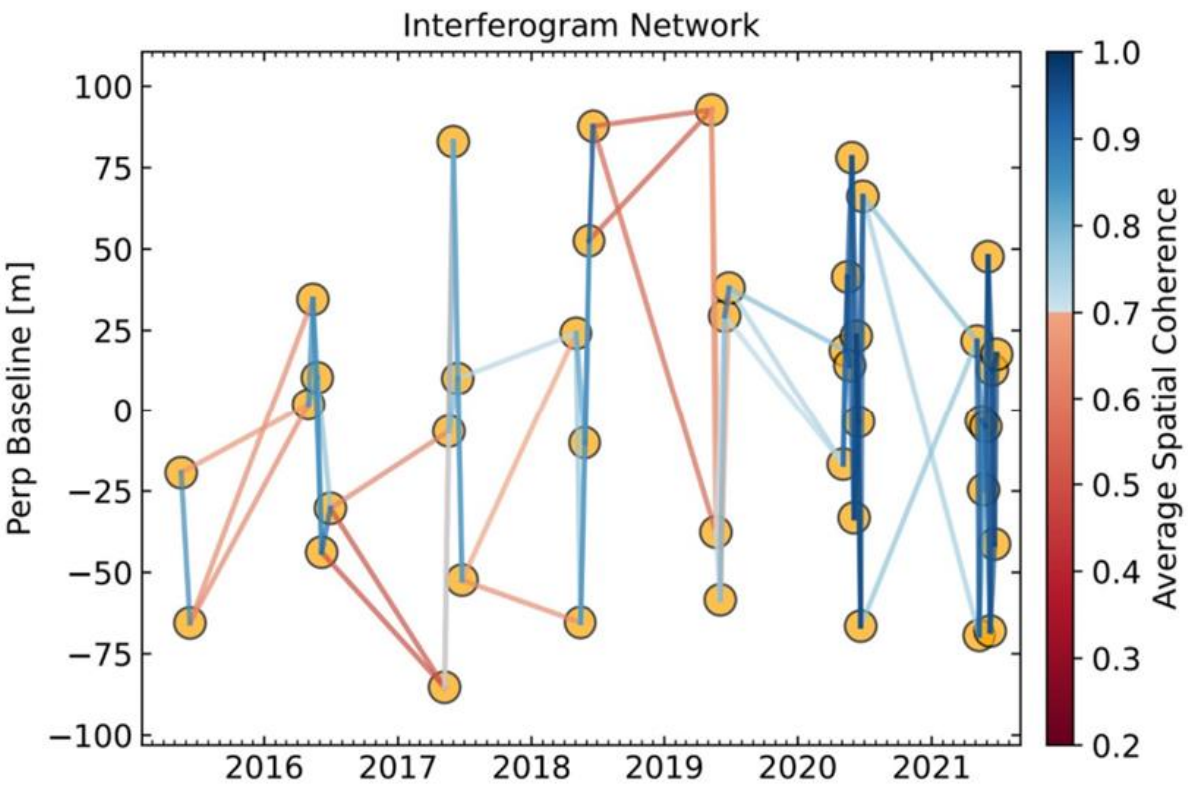

Figure 9. A reduced set of approximately yearlong interferograms. The x-axis is time in years, and the y-axis is perpendicular baseline. The lines represent individual interferograms. The dots are SAR acquisitions, and the red lines are interferograms where the majority of the data was unusable due to the spatial coherence being too low, while the blue lines represent interferograms with mostly usable data. Although some of the interferograms were low in coherence, more of them had high enough coherence to be useful in calculating the final time series result.

Much of the InSAR signal in highly vegetated regions such as northern New Mexico is dominated by the effects of humidity (long-wavelength noise) and snow or vegetation (reduced

spatial correlation at short wavelengths). Choosing only interferograms from dates that are not as highly impacted by these sources of noise can help us avoid coherence issues; therefore, for Valles as well as Long Valley this can allow for a more stable time series result. These criteria resulted in only 37 usable interferograms.

The final time series shows broad subsidence across the entire region of less than 1 cm/yr (Figure 10). This includes the Pajarito, Nacimiento, and Gallina fault zones. This deformation is not confined to the caldera, and appears to be more regional. We estimate the uncertainty is around 1 mm/yr for this type of processing (Havazli and Wdowinski, 2021). Based on the final time series results, no caldera-specific deformation is observed.

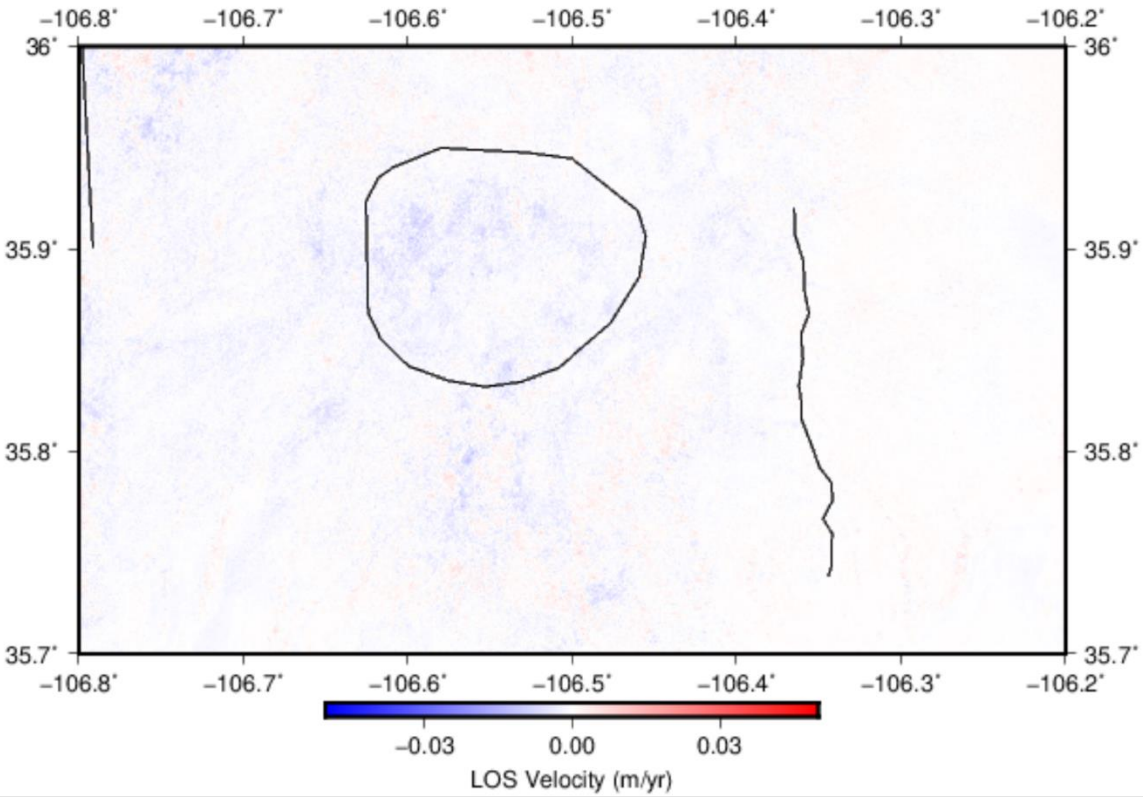

Figure 10. Line-of-sight (LOS) velocity over the Valles caldera created using a linear fit to the Mintpy time series, from 2014 to 2022. The caldera ring fracture zone and the main section of the Pajarito Fault trace (left) and the Gallina fault traces (right) are indicated in black.

2.3 GNSS Processing

Our GNSS data includes 13 stations first installed and surveyed during October 2002, some of which were also surveyed in 2003, and all of which we resurveyed in 2022. The fieldwork included going to the Valles caldera in October 2022 and installing 6 Trimble 5700 GPS receivers with Zephyr geodetic antennas, using a 13.05 cm spike mount placed directly on the geodetic monuments (Figure 11). After 3-4 days, the receivers were collected and re-deployed at a different set of sites. The data collection dates and time lengths are shown in Table 1.

Table 1. Station name, days running, longitude, and latitude for each station in the survey.

GPS Station Name	Day installed	Day Retrieved	Longitude	Latitude
1. CNCH	**276**	**280**	**-106.52524**	**35.81356**
2. VCDM	**276**	**280**	**-106.44443**	**35.88193**
3. VCJC	**276**	**280**	**-106.53038**	**35.91059**
4. VCSA	**276**	**280**	**-106.53286**	**35.96712**
5. VCVG	**276**	**280**	**-106.49529**	**35.8391**

6. VCVS	**277**	**279**	**-106.58978**	**35.93701**
7. FENT	**283**	**293**	**-106.67426**	**35.88151**
8. QMZN	**293**	**299**	**-106.34041**	**35.89353**
9. TA33	**291**	**298**	**-106.24521**	**35.77749**
10. VCCC	**283**	**293**	**-106.56604**	**35.83649**
11. VCHQ	**283**	**287**	**-106.53303**	**35.86096**
12. VCSS	**283**	**293**	**-106.61173**	**35.90917**
13. VCSW	**283**	**287**	**-106.56893**	**35.89426**

Figure 11. Field photos taken during the GPS survey in October 2022. Clockwise from the top left: sites VSVS, CNCH, VCCC, and QMZN.

The majority of the stations had usable data; however, station VCCC was knocked over (potentially by a storm or animal) during Julian days 286 and 287 (Figure 12), but none of the other stations had to have days removed from the processing (Figure 13). This station was set back up after day 287 and ran for 5 days following this, so those 2 days were the only ones that had to be thrown out for this station. We removed these days by removing the Rinex files (Figure 14) for both days for station VCCC. Station VCVS also did not run for the last day that we had it out due to being overturned, possibly from an animal. But because it simply stopped collecting

data after this occurred, we did not have to remove any days for VCVS. The fieldwork itself involved finding the small steel benchmarks where the stations had previously been installed in the 2002-2003 surveys, installing the receivers and antennas and ensuring the antenna was level and centered over the benchmark, using a compass to make sure the “North” arrow was pointing to the North. Then, we took note of the serial numbers of the equipment, connected the receiver to the antenna and battery, and powered it on. On recovery of the site we repeated the steps in reverse order and recorded whether the site was still operating and level. The raw data had to be converted to RINEX (receiver independent exchange) format to be processed, using the Trimble software “Convert to RINEX” (Figure 14)

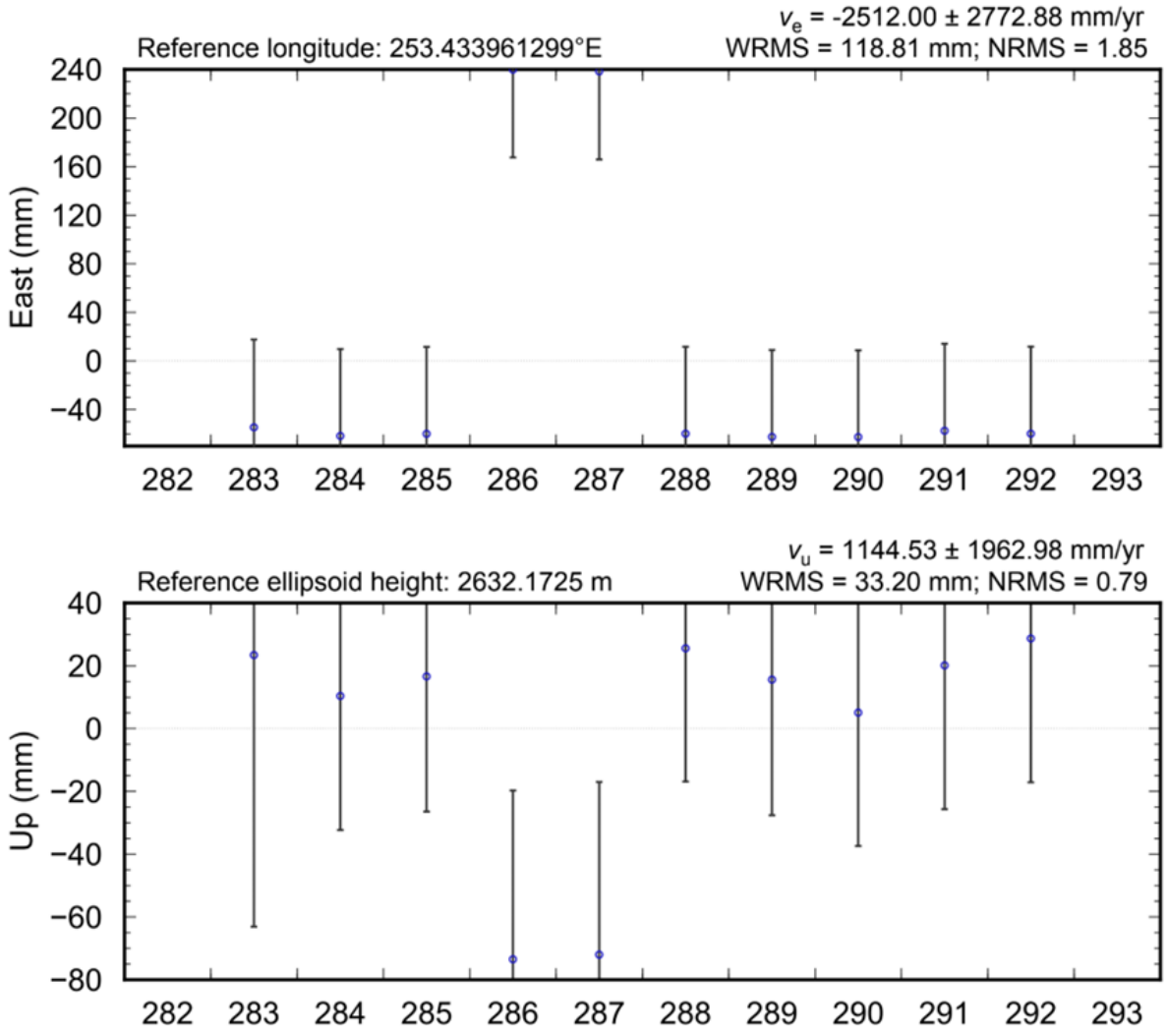

Figure 12. GLOBK-generated figure for station VCCC from early in the processing. Days 286 and 287 are significantly different than the other days, likely due to being knocked over by a storm. This was then set back up on day 288, and then the station recorded data successfully for 5 more days. To resolve this issue, we removed the Rinex file for this station for both of the affected days and re-processed the data in GAMIT/GLOBK.

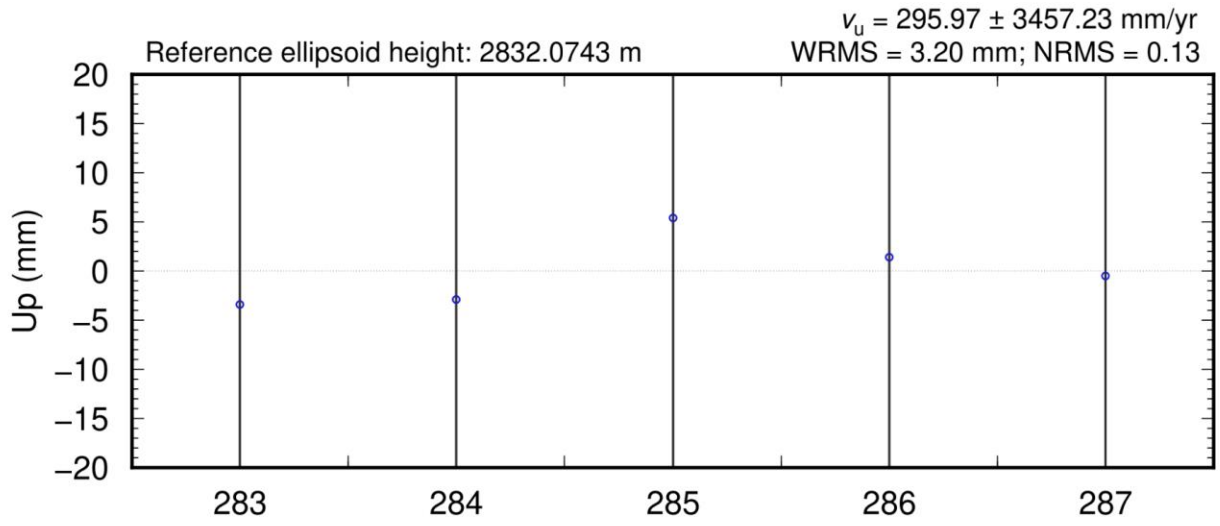

Figure 13. GLOBK-generated figure for station VCSW from early in the processing. The velocity has significant error because this is prior to combining the results from the 2002 and 2003 data, as well as using the continuous sites in the double differencing technique; however, this shows that this station ran for the full time span with no significant issues.

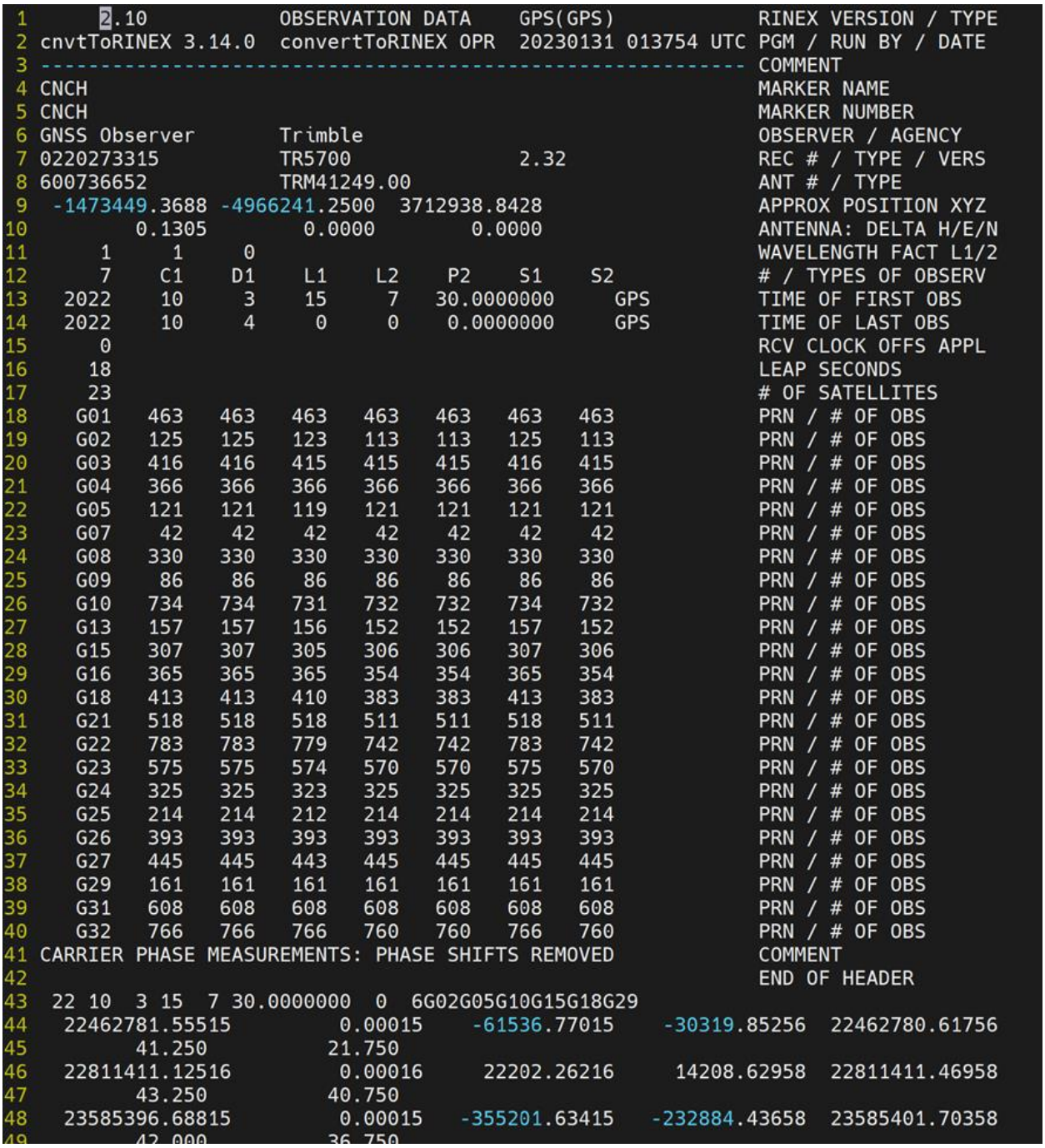

```
     2.10           OBSERVATION DATA    GPS(GPS)            RINEX VERSION / TYPE
cnvtToRINEX 3.14.0  convertToRINEX OPR  20230131 013754 UTC PGM / RUN BY / DATE
------------------------------------------------------------ COMMENT
CNCH                                                         MARKER NAME
CNCH                                                         MARKER NUMBER
GNSS Observer       Trimble                                  OBSERVER / AGENCY
0220273315          TR5700              2.32                 REC # / TYPE / VERS
600736652           TRM41249.00                              ANT # / TYPE
 -1473449.3688 -4966241.2500  3712938.8428                   APPROX POSITION XYZ
        0.1305        0.0000        0.0000                   ANTENNA: DELTA H/E/N
     1     1     0                                           WAVELENGTH FACT L1/2
     7    C1    D1    L1    L2    P2    S1    S2            # / TYPES OF OBSERV
  2022    10     3    15     7   30.0000000     GPS         TIME OF FIRST OBS
  2022    10     4     0     0    0.0000000     GPS         TIME OF LAST OBS
     0                                                       RCV CLOCK OFFS APPL
    18                                                       LEAP SECONDS
    23                                                       # OF SATELLITES
   G01   463   463   463   463   463   463   463            PRN / # OF OBS
   G02   125   125   123   113   113   125   113            PRN / # OF OBS
   G03   416   416   415   415   415   416   415            PRN / # OF OBS
   G04   366   366   366   366   366   366   366            PRN / # OF OBS
   G05   121   121   119   121   121   121   121            PRN / # OF OBS
   G07    42    42    42    42    42    42    42            PRN / # OF OBS
   G08   330   330   330   330   330   330   330            PRN / # OF OBS
   G09    86    86    86    86    86    86    86            PRN / # OF OBS
   G10   734   734   731   732   732   734   732            PRN / # OF OBS
   G13   157   157   156   152   152   157   152            PRN / # OF OBS
   G15   307   307   305   306   306   307   306            PRN / # OF OBS
   G16   365   365   365   354   354   365   354            PRN / # OF OBS
   G18   413   413   410   383   383   413   383            PRN / # OF OBS
   G21   518   518   518   511   511   518   511            PRN / # OF OBS
   G22   783   783   779   742   742   783   742            PRN / # OF OBS
   G23   575   575   574   570   570   575   570            PRN / # OF OBS
   G24   325   325   323   325   325   325   325            PRN / # OF OBS
   G25   214   214   212   214   214   214   214            PRN / # OF OBS
   G26   393   393   393   393   393   393   393            PRN / # OF OBS
   G27   445   445   443   445   445   445   445            PRN / # OF OBS
   G29   161   161   161   161   161   161   161            PRN / # OF OBS
   G31   608   608   608   608   608   608   608            PRN / # OF OBS
   G32   766   766   766   760   760   766   760            PRN / # OF OBS
CARRIER PHASE MEASUREMENTS: PHASE SHIFTS REMOVED             COMMENT
                                                             END OF HEADER
 22 10  3 15  7 30.0000000  0  6G02G05G10G15G18G29
  22462781.55515         0.00015    -61536.77015    -30319.85256  22462780.61756
        41.250          21.750
  22811411.12516         0.00016     22202.26216     14208.62958  22811411.46958
        43.250          40.750
  23585396.68815         0.00015   -355201.63415   -232884.43658  23585401.70358
        42.000          36.750
```

Figure 14. Station VCVS Rinex file used in the Gamit and GLOBK processing. This file format is rigid and must have correct information prior to being used in processing, or there will be (often significant) error in the final results. Or potentially, the processing will not work at all and no final result can be calculated until the Rinex file is fixed.

To precisely determine the coordinates and velocities of the survey GNSS sites, nearby continuous GNSS reference sites must be used. Using the double-difference approach, the atmospheric delays between GPS satellites and the sites can be made to cancel out (assuming that the troposphere is the same between each site), allowing determination of the exact distance between these continuous sites and the survey sites. From these 'baseline' solutions, the exact coordinates and velocities of the survey sites can then be calculated.

We processed this data using the free software GAMIT (GNSS At MIT) and GLOBK (Global Kalman filter) (Herring et al., 2018). We converted the raw data into RINEX (Receiver Independent Exchange) files using the Trimble "Convert to Rinex" software, which provides the GPS observations in a standard ASCII format, usable in our processing steps (Defraigne and Petit, 2003). We then set up a folder with the year we were processing (2002, 2003, and 2022), and downloaded the RINEX files for a set of IGS sites across North America (Figure 15). We then ran GAMIT for each group of days, which prepares the data, prepares the batch control, integrates GPS satellite orbits, calculates modeled phase, and takes the derivative of that with respect to velocity and position parameters, and estimates parameters using a least squares technique to create an h-file containing the baseline solutions (distances between sites) for input to GLOBK (Herring et al., 2018).

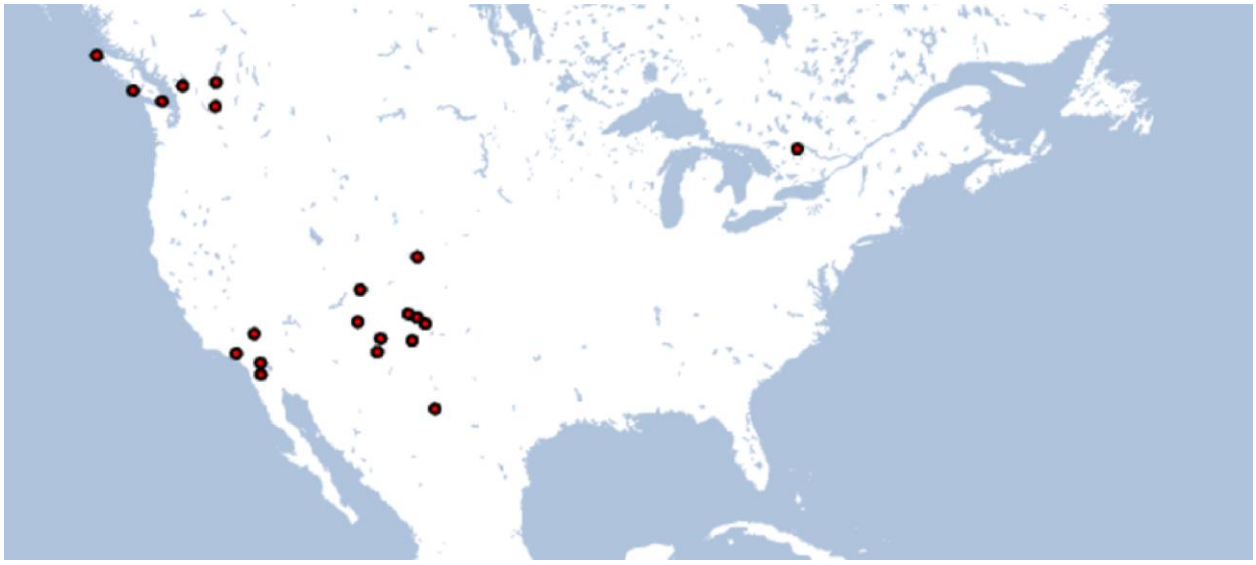

Figure 15. A map showing the locations of all IGS sites used in the GPS processing. Map created using Generic Mapping Tools.

We then used GLOBK to create combined solutions for different years and generate position and velocity solutions for each site. GLOBK uses the known relative distances and velocities of the IGS sites to estimate precise time series and velocities for each survey site (Figures. 16 and 17). The final results indicate -1.24 mm/yr of vertical deformation in our study area (Figure 18). The average horizontal motion is 6.16 mm/yr to the South and 13.80 mm/yr to the west, which can be explained by the tectonic motion in the region (Murray et al., 2019) (Figure 14).

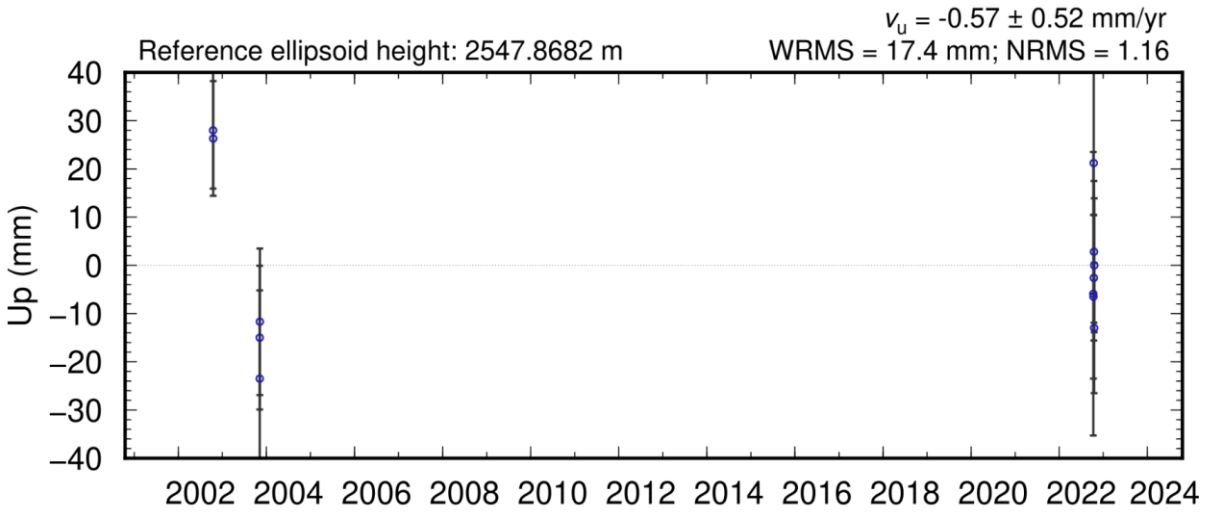

Figure 16. GLOBK generated figure for station VCSS, showing vertical motion of -0.57 mm/yr. The error is ±0.52 mm/yr, which is nearly equal in magnitude to the vertical motion.

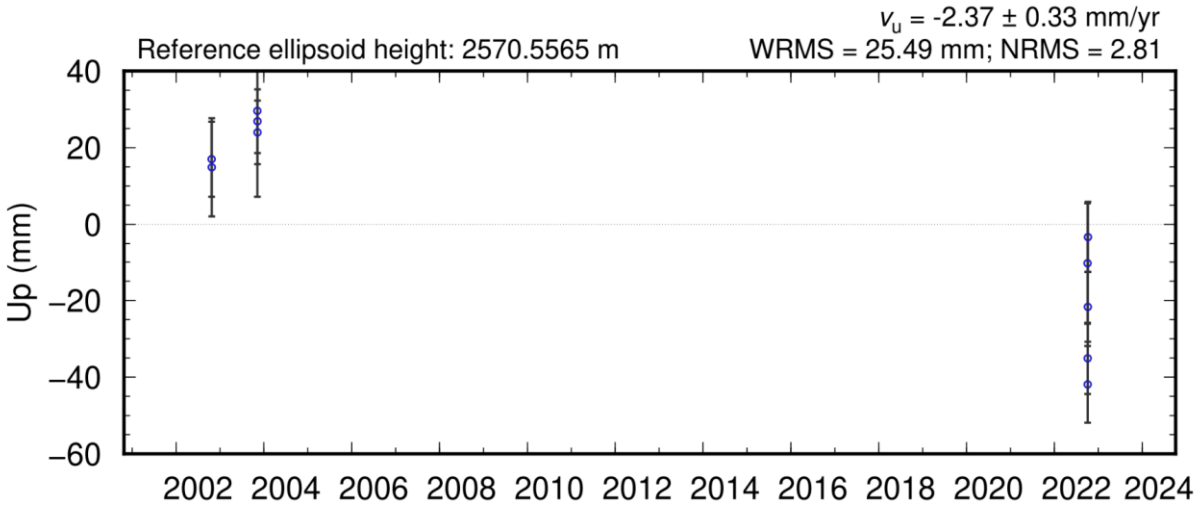

Figure 17. GLOBK generated figure for station CNCH, showing vertical motion of -2.37 mm/yr. The error for this station is ±0.33 mm/yr.

In order to remove regional deformation associated with Northern New Mexico (Figures. 18,19), we used station TA33 as a reference station (Figures. 20, 21). This is the station furthest

away from the caldera, and the most representative of the regional motion rather than motion directly related to the caldera. However, any impacts from nearby sources of deformation may introduce more error; this is the case in any reference station, so the reference station should be chosen carefully such that no new effects are added to the other stations' velocity results. The vertical average vertical velocity once these regional effects are removed is 0.06 mm/yr, while the horizontal average velocity is 1.13 mm/yr to the south and 0.1 mm/yr to the west.

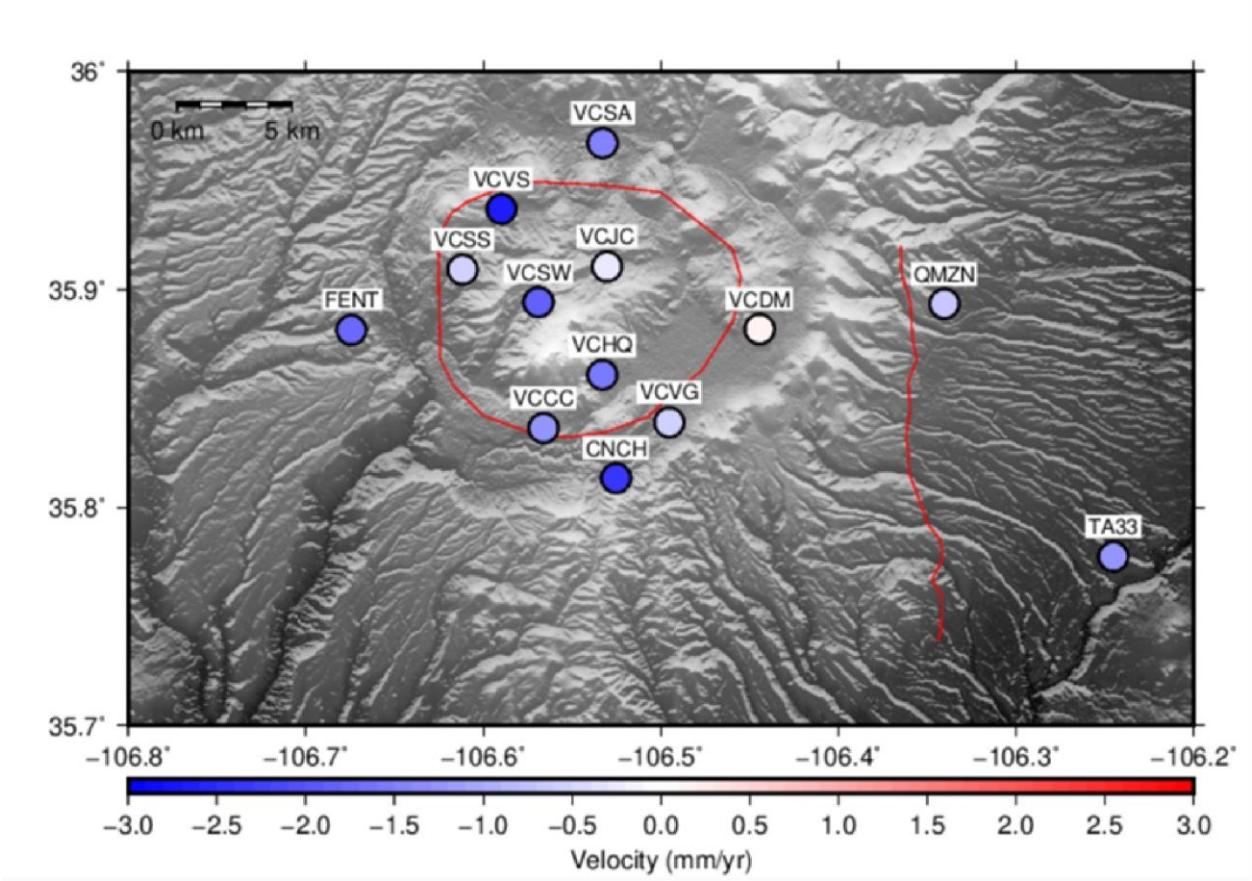

Figure 18. The 13 GPS stations processed from 2002-2022 with the GLOBK-calculated velocities indicated. The average velocity (vertical deformation) is -1.24 mm/yr. The reference frame used is the International Terrestrial Reference Frame 2014 (IRTF2014). The majority of these stations show subsidence, with the strongest signal in stations VCVS and CNCH.

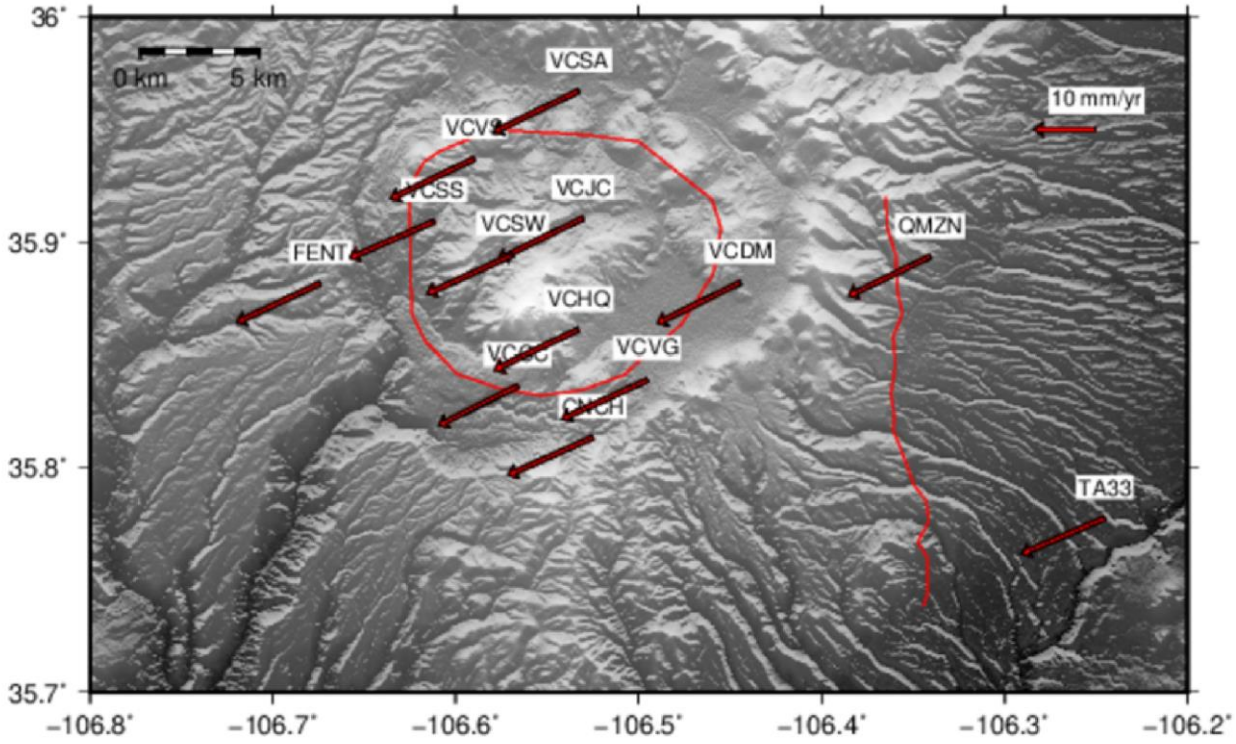

Figure 19. The 13 GPS stations processed from 2002-2022 with the GLOBK-calculated horizontal velocities indicated. The average horizontal motion is 6.16 mm/yr to the south and 13.80 mm/yr to the west. The arrow labeled “10 mm/yr" is for scale. The reference frame used is the International Terrestrial Reference Frame 2014 (ITRF2014). All of these are pointing in the same general direction, and the majority of this deformation is likely to be regional and not specific to the caldera.

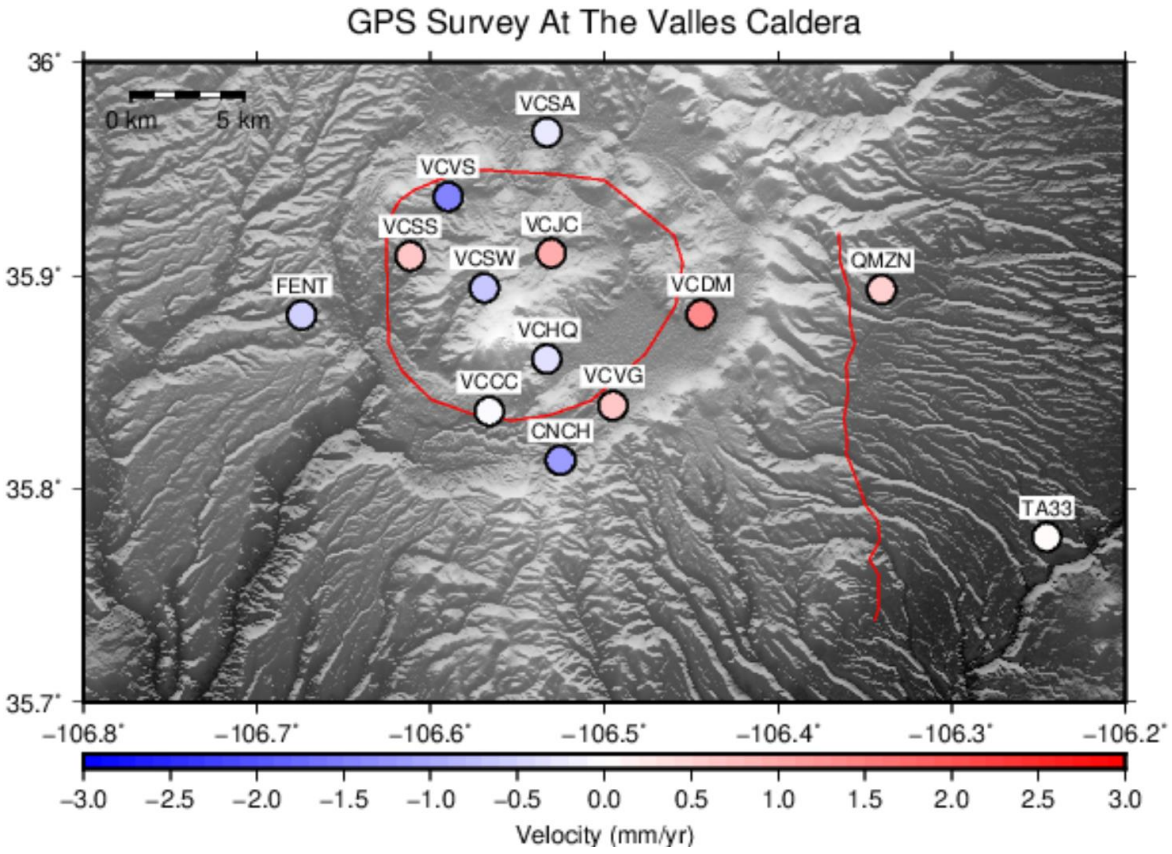

Figure 20. The 13 GPS stations processed from 2002-2022 with the GLOBK-calculated velocities indicated. The average velocity (vertical deformation) is 0.06 mm/yr. These velocities are in relation to station TA33 (indicated on Figure 18). See supplement for figures with all stations used as reference stations. The magnitude of the majority of these stations is less than the average GLOBK-calculated error, which is ±0.43 mm/yr.

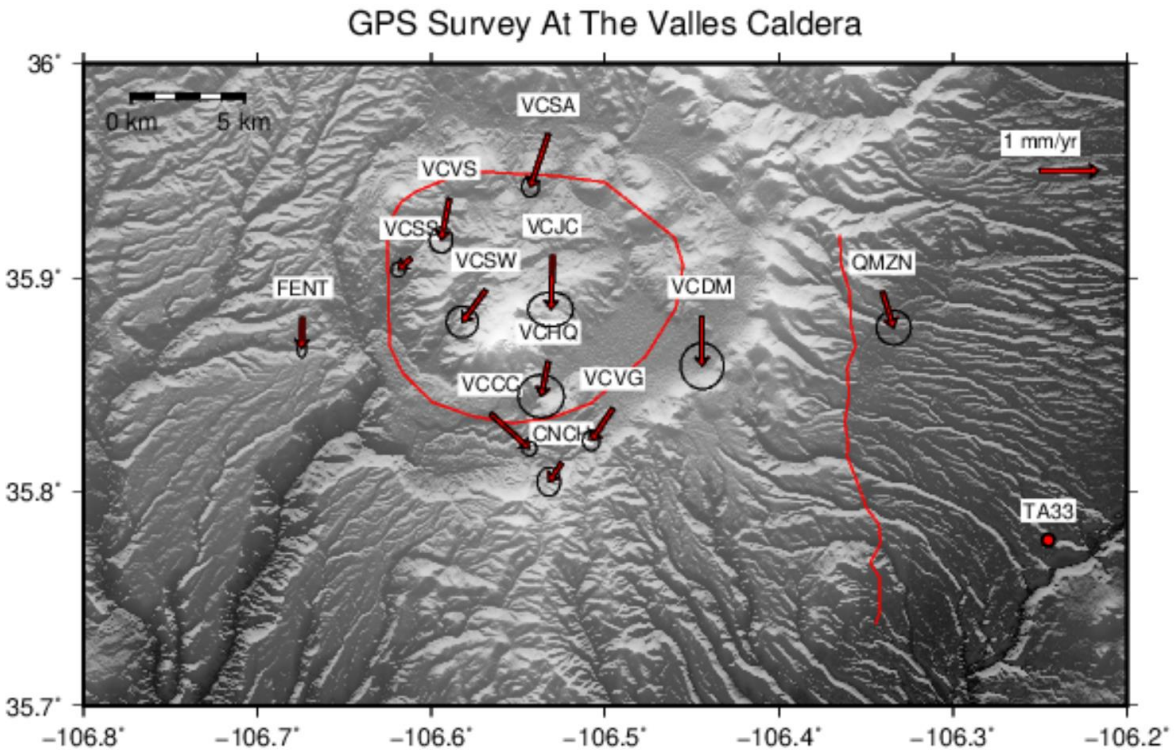

Figure 21. The 13 GPS stations processed from 2002-2022 with the GLOBK-calculated horizontal velocities indicated. The average horizontal motion is 1.13 mm/yr to the south and 0.1 mm/yr to the west. The arrow labeled "1 mm/yr" is for scale. These velocities are in relation to station TA33 (indicated on Figure 18). See supplement for figures with all stations used as reference stations.

2.4 Mogi model results

We use GPS results to model displacement within the Valles Caldera. There are significant limitations due to the lack of data (including the 19-year long gap in GPS surveys), the error associated with the data, and the lack of spatial density. But given the data we have, the Mogi model is a relatively simple way of modeling the data, and could be a good starting point

for future models when more data is acquired. Using a grid search, we varied depth, location, and volume change, minimizing the reduced chi squared value between the model data and the observed GPS data.

The results are shown in table 2 (with a portion of the varying chi-squared values in Figures 25 and 26), and the location of the results are shown in Figure 24. The results for each individual station and the residuals are shown in Figures 22 and 23. Poisson's ratio in this model is 0.25, which is typical for a rhyolitic composition (Meister et al., 1980). We chose a range of 0-15 km for the depth, a location range of ~10 km (5 km to the West, East, North, and South of the center of the caldera), and a volume range of -0.01 to 0 km^3/yr for the grid search. We decided to only model the subsidence within the observations. This is because the majority of the observations show subsidence, and with the small magnitude of the vertical motion, it is unlikely that the uplift seen is anything more than noise. And because the majority of the observations are probably noise and not real deformation, it is not reasonable to model anything more complicated than a single point source.

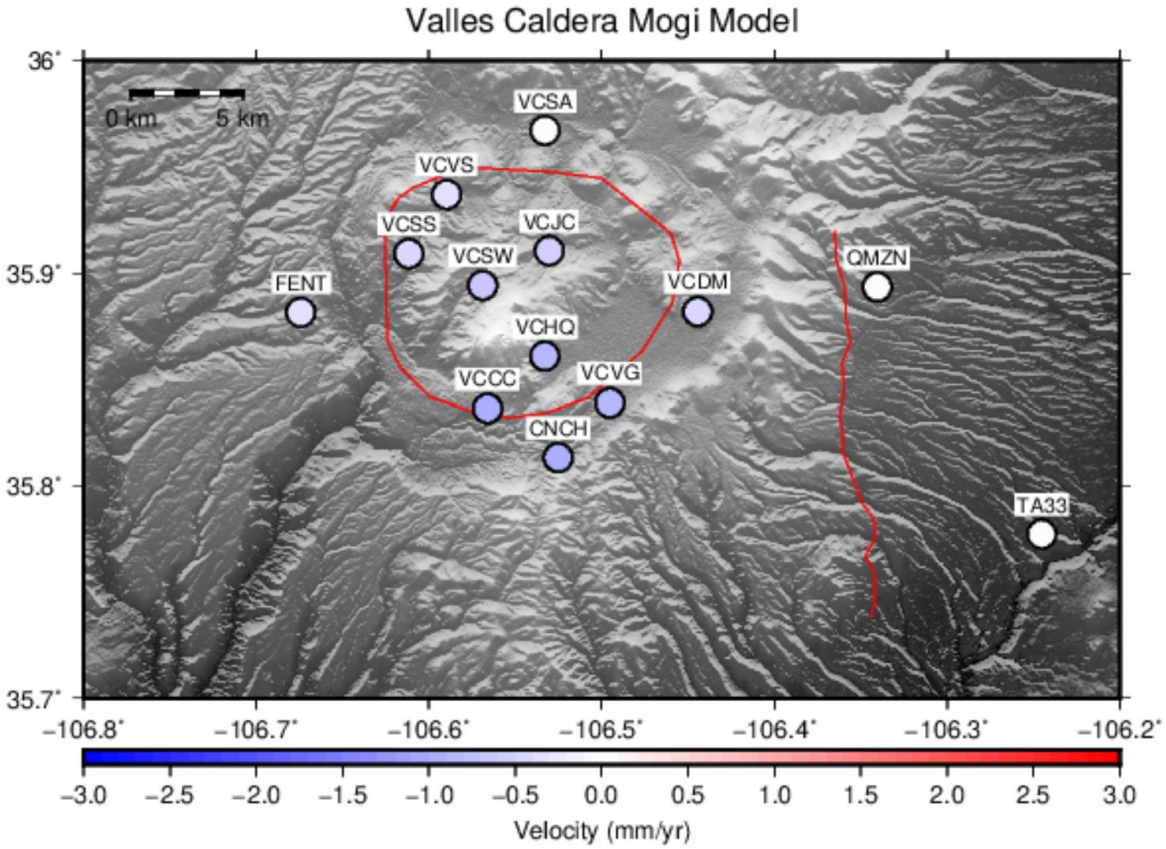

Figure 22. Results from the Mogi (1958) model. The source is closest to CNCH, where the subsidence is the highest in the observations. The magnitude of the velocity decreases radially from the source.

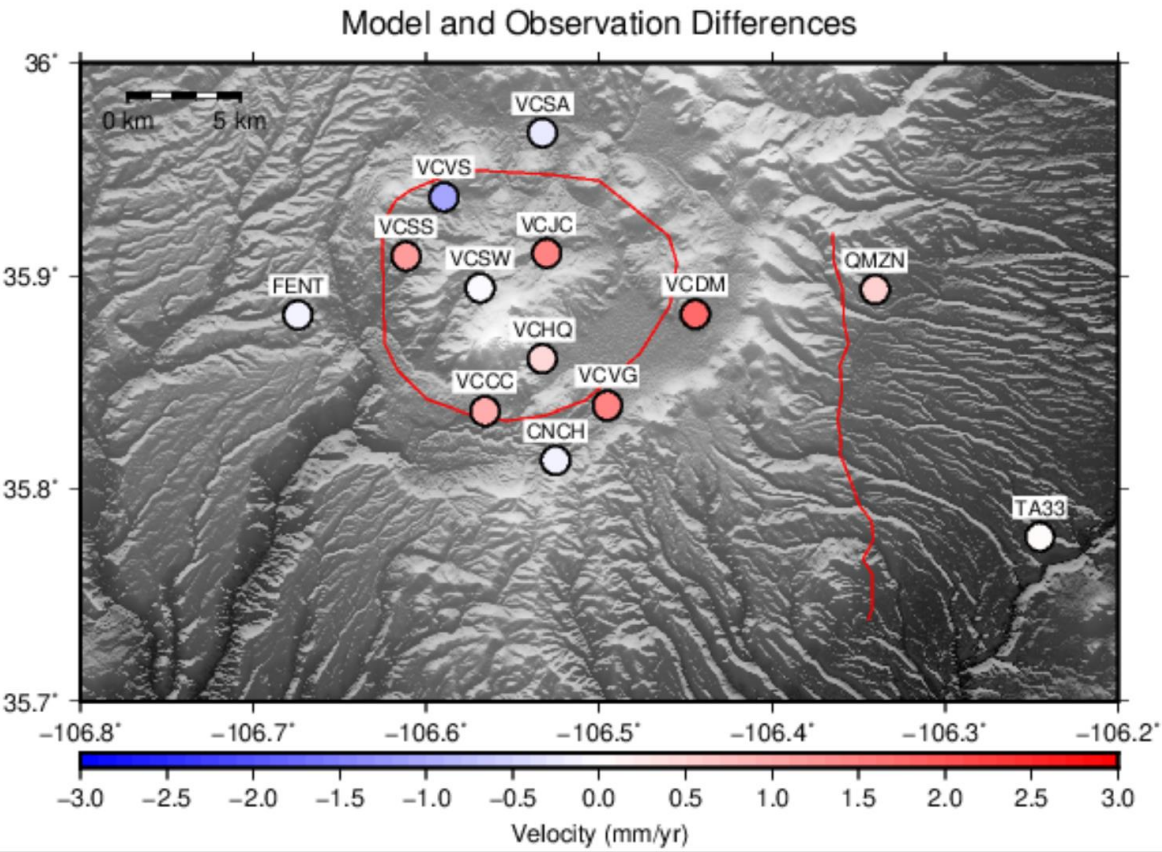

Figure 23. The residuals from the Mogi (1958) model compared to the GPS results. As expected, the highest residuals are in the stations that were uplifting the most (VCDM and VCJC), while the lowest residual is CNCH, which is closest to the best-fitting source.

Table 2. The best-fit parameters from the Mogi (1958) model of the GPS observations of the Valles caldera.

Parameter	**Value**
Depth (km)	12
Volume (km^3)	$-8.2*10^{-3}$

Longitude	35.8181
Latitude	-106.5457

Figure 24. The location of the best-fit Mogi source. This is closest to the station “CNCH,” which has the highest rate of subsidence in the GPS observations.

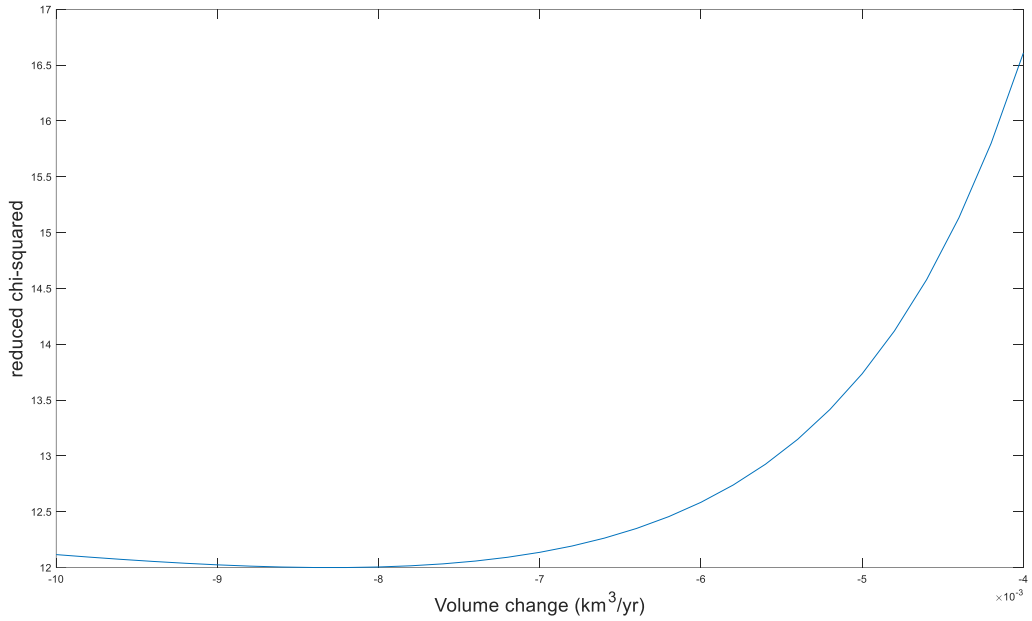

Figure 25. Chi squared vs. volume change of the model parameters. The best fitting volume change is -8.2*10^{-3} km^3/yr.

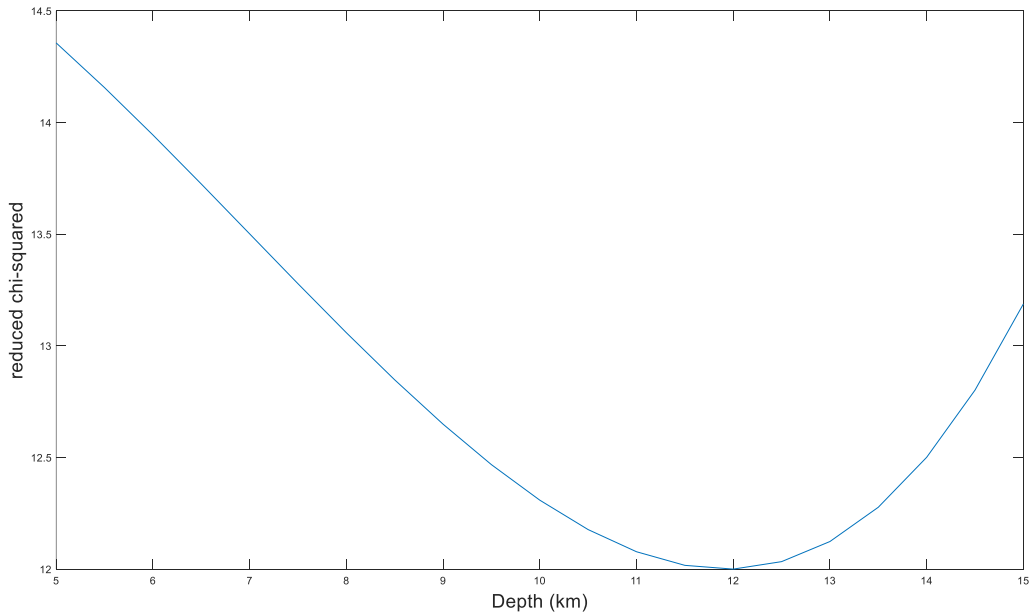

Figure 26. Chi squared vs. depth of the model parameters. The best fitting depth is 12 km.

2.5 Long Valley

The GNSS data from the Long Valley caldera shows a stronger signal than what is seen in the Valles caldera. The velocities observed are orders of magnitude larger than the velocities observed in Valles (with the station TA33 reference frame).

As a result, the data from the Long Valley caldera can be reasonably fit with more complex models, as there is measurable deformation in the region. One example of this is Liu et al., 2011, where they fit both InSAR and GNSS data to both a Mogi source and a more complex "Dipping prolate spheroid" source, with more parameters (Figure 29). This is largely possible because there is a strong enough signal in the Long Valley data to indicate an individual source that is directly related to the caldera itself, and is not simply regional subsidence or uplift.

We processed InSAR data using similar methods to the processing steps for the Valles caldera. We used year long interferograms, ISCE, and essentially the same processing steps but with a different region of interest (Figure 27). We also plotted some of the GNSS data within the caldera (Figure 28), which also shows a strong uplift signal.

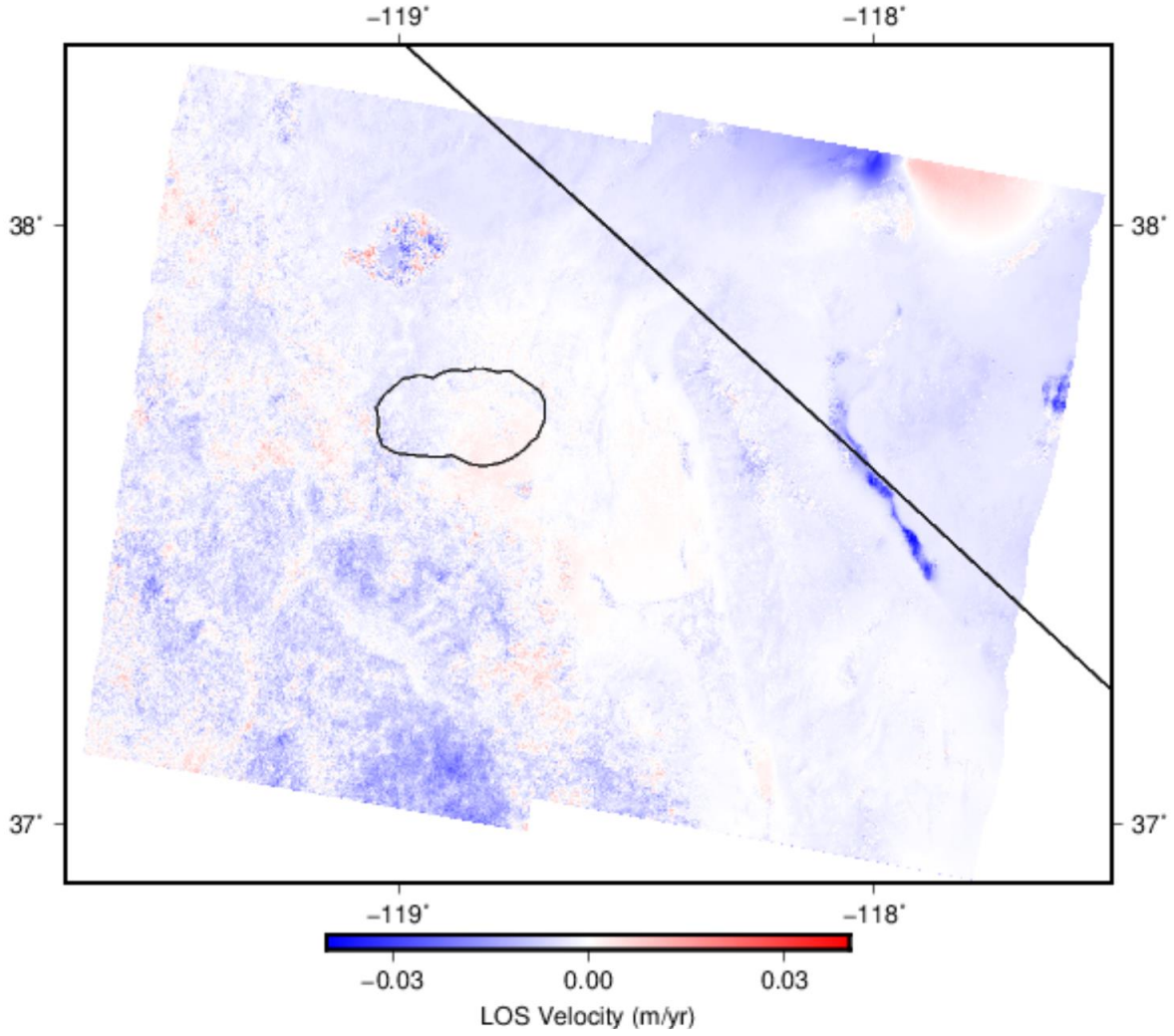

Figure 27. MintPy-generated line-of-sight velocities for the Long Valley Caldera. The ring fracture is indicated in black. The majority of the region shows little motion, with uplift indicated in red within the ring fracture.

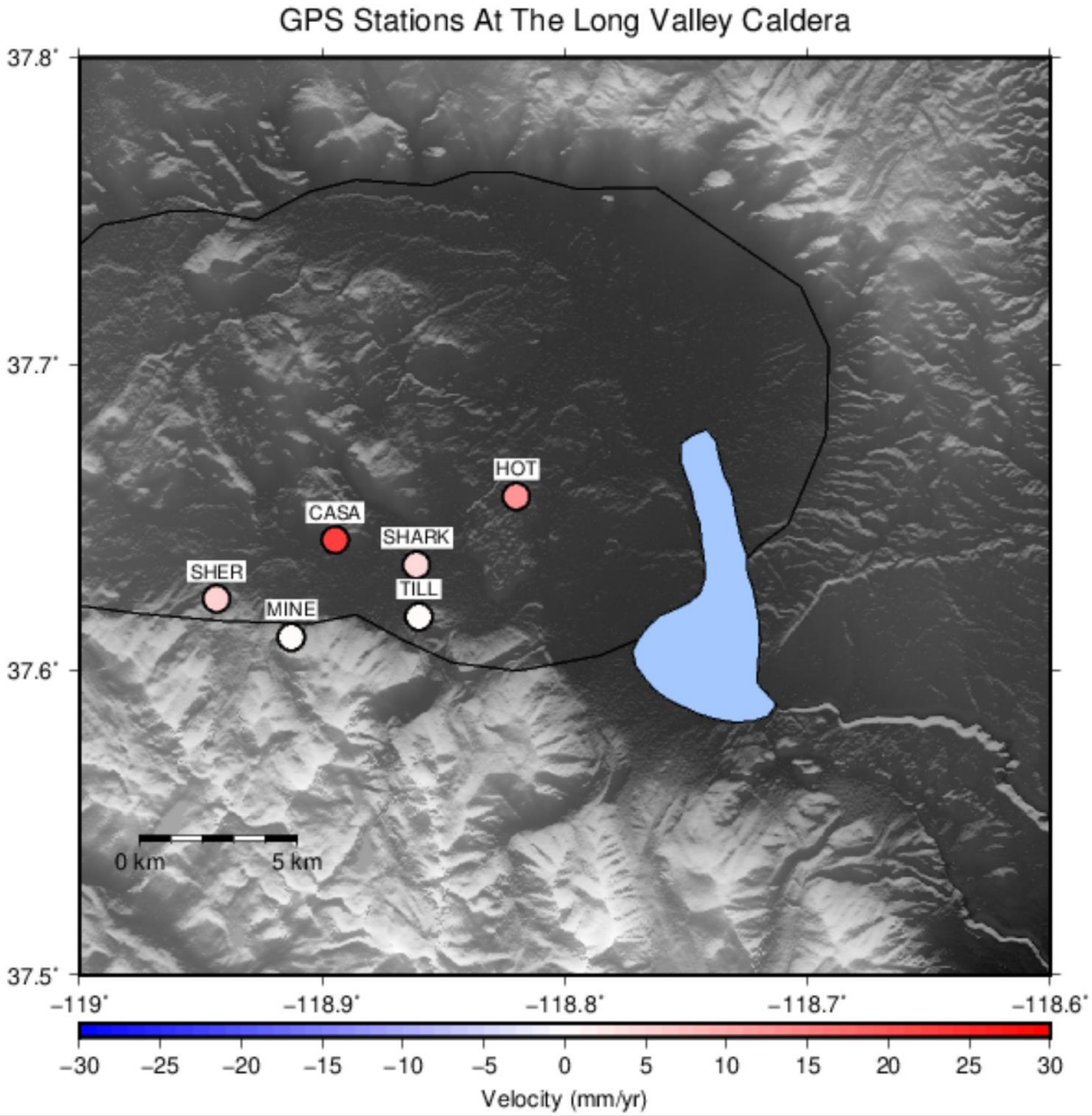

Figure 28. Continuous GNSS stations and their velocities at the Long Valley caldera (Battaglia et al., 2003).

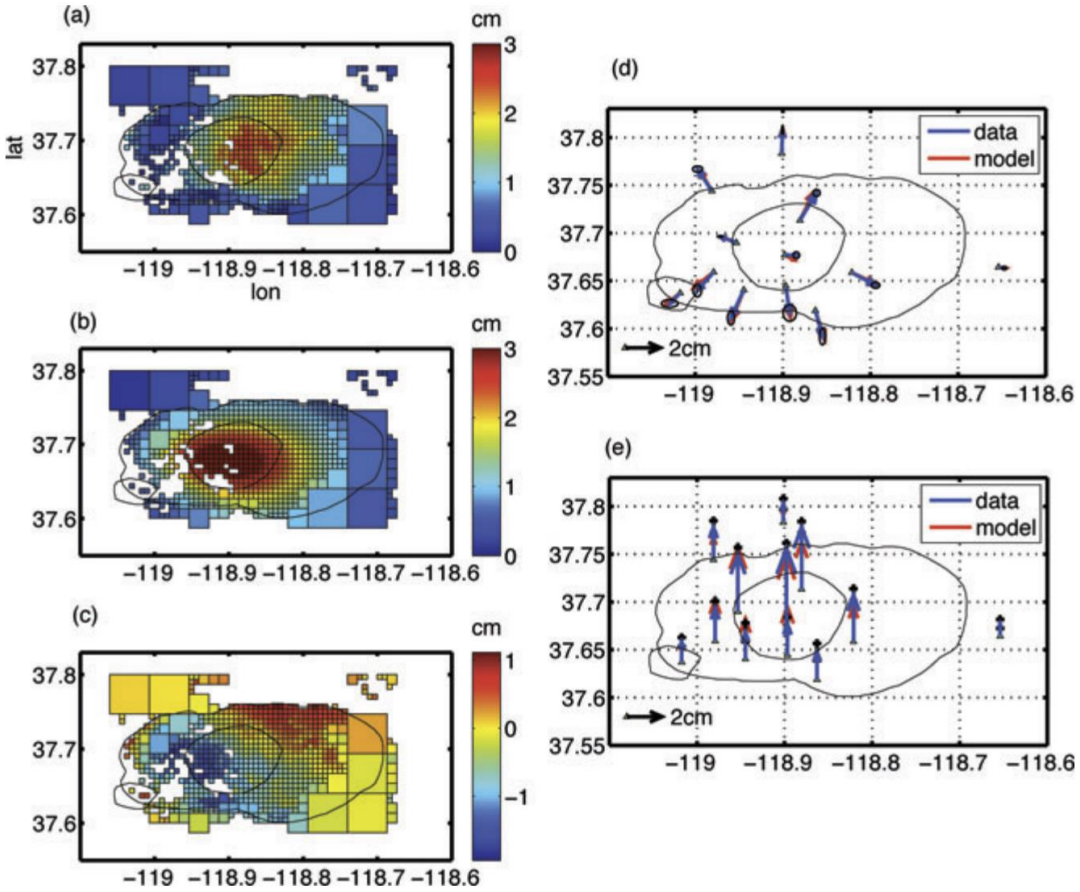

Figure 29. Model data from Liu et al., 2011.

3. DISCUSSION:

Both the InSAR and GPS results indicate subsidence across the Valles caldera. However, this subsidence appears across the entire region, and is not specific to the caldera. There are multiple reasonable hypotheses that could explain this, with several being more likely when considering additional studies and other information. However, with the vertical rates being <2 mm/yr, which is within the range of noise uncertainty of ±0.43 mm/yr, it is difficult to definitively identify the source of this motion.

3.2 Fluid Migration

Waite and Smith (2002) argue that recent subsidence in Yellowstone is a result of hydrothermal fluid migration. Valles has a known hydrothermal system that formed at around the same age as the caldera itself (Goff and Shevenell, 1987). Parts of this hydrothermal system discharge into the nearby Jemez River, which could cause a subsidence pattern in the region if the discharge rate exceeds recharge from precipitation (Goff and Shevenell, 1987; Goff et al., 1988). If hydrothermal fluid movement is the cause of the surface deformation seen in the geodetic data presented here, it is likely unrelated to the seismically observed low velocity zone (Wilgus et al., 2023), as 10 km (which Wilgus et al., 2023 indicated as the highest depth of the low velocity zone) is not a reasonable depth for a body of significant hydrothermal fluid (Stimac et al., 2015).

The hydrothermal fluid within the Valles caldera is also presently degassing (Goff and Janik, 2002; Blomgren et al., 2019), releasing primarily 99% steam, and lesser amounts of CO_2, H_2S, and other geothermal gas components. Degassing also causes the types of vertical motion that we observe, and this explanation can potentially explain the regions of the highest subsidence, which are near several springs associated with hydrothermal fluid movement. Thus, if we choose to draw a conclusion based on the geodetic data, hydrothermal degassing is the most likely explanation, as we have evidence of degassing based on previous studies such as Blomgren et al., (2019).

3.3 Magma crystallization

Another study at Yellowstone shows that models fit to subsidence observations are likely due at least in part to magma crystallization (Dzurisin et al., 1990). If a shallow magma body is crystallizing beneath the Valles caldera, this may also have an impact on the movement of

groundwater above the crystallized portion of the subjacent pluton (Goff and Grigsby, 1982; Goff et al., 1988). This could also explain why there is both subsidence (cooling magma tends to contract) as well as a seismic low-velocity zone, as portions of the magma would still be liquid. However, the imaged low-velocity zone is localized beneath Redondo peak near the center of the caldera (Wilgus et al., 2023), so subsidence associated with magma crystallization does not fully explain the broad pattern of observed deformation (Figures. 10 and 20). And the horizontal motion observed does not have a significant inward component pointing to a magmatic source, so this explanation is less likely.

3.4 regional subsidence

The Pajarito fault zone is a normal fault east of the Valles caldera, striking north to south (Broxton and Vaniman, 2005**).** Although it is a complex fault system, the entire region east of the fault zone is part of the RGR and has been deforming for the last 25 Myr (Reilinger and York, 1979). Overall, subsidence due to rifting is estimated at <1 mm/yr (Figure 25) (Murray et al., 2019). This likely accounts for at least a portion of the deformation we observed in Valles caldera, but more work is needed to determine whether the rates and pattern of subsidence within Valles are significantly greater and independent of the regional processes.

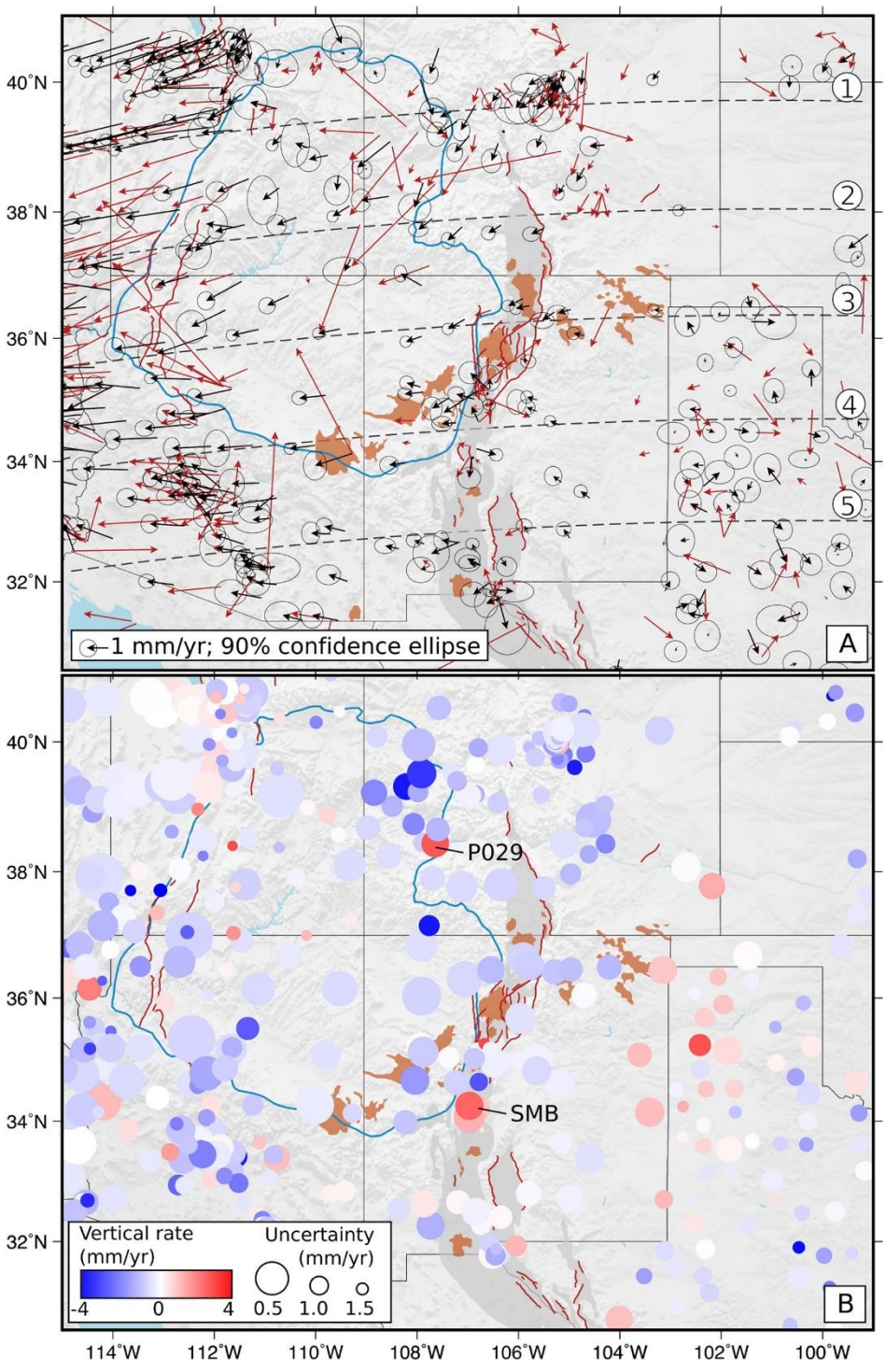

Figure 30. GPS processing results from Murray et al., (2019), showing broad subsidence in the Rio Grande rift and Colorado Plateau. The majority of this region is subsiding, with the most notable anomaly being the Socorro Magma Body (indicated by "SMB" in the figure).

3.5 Changes in rainwater mass

Small signals of ground motion can sometimes be related to changes in annual precipitation. While there has been little change in annual precipitation in the Valles caldera region (Coop and Givnish, 2007), these small changes could potentially have an impact on the ground motion observed using geodetic methods.

4. CONCLUSIONS:

In this study, we present updated GNSS and new InSAR observations within the Valles caldera spanning the last several decades suggest a broad pattern of subsidence at rates of 1 – 2 mm/yr. The total rates of deformation seen in both InSAR and GNSS results are consistent but small and could be explained by measurement error associated with both of these methods. The GNSS data also have a 19-year gap in the observations between 2003-2022, limiting our ability to detect any variations in the rates of motion. We show that our best InSAR observations from using year-long interferograms can potentially still include noise due to the high topography and dense vegetation within Valles. We suggest degassing of hydrothermal fluids from the caldera-hosted geothermal system can explain the deformation from our observations, but more geodetic observation can help resolve the potential source of deformation.

In the future, installation of continuous GNSS monitoring stations within the Valles caldera would greatly improve our ability to detect ongoing deformation, especially in regions of high hydrothermal fluid movement and around Redondo Peak. Currently, no continuous GPS stations are available within the general region. Although our results do not suggest Valles represents a significant volcanic hazard at this time, observations from the better monitored Yellowstone and Long Valley calderas indicate that geodetic signals within calderas are highly

variable and can change from hardly active to very concerning relatively quickly (Dzurisin et al., 1990). The Valles caldera is located 30 km west of the city of Los Alamos and home to Los Alamos National Laboratory. Based on studies of past volcanism (Wolff and Gardner, 1995), it is reasonable to assume that any future eruptions would be comparatively large ($\geq$10 km^3) and disruptive. It is in the best interest of the communities within and around this region to have Valles caldera continuously monitored to refine our understanding of volcanic hazards in New Mexico.

REFERENCES:

Bailey, R. A., Dalrymple, G. B., & Lanphere, M. A. (1976). Volcanism, structure, and geochronology of Long Valley Caldera, Mono County, California. *Journal of Geophysical Research*, *81*(5), 725–744. https://doi.org/10.1029/JB081i005p00725

Bamler, R., & Hartl, P. (1998). Synthetic aperture radar interferometry. *Inverse Problems*, *14*(4), R1–R54. https://doi.org/10.1088/0266-5611/14/4/001

Battaglia, M., Segall, P., & Roberts, C. (2003). The mechanics of unrest at Long Valley caldera, California. 2. Constraining the nature of the source using geodetic and micro-gravity data. *Journal of Volcanology and Geothermal Research*, *127*(3–4), 219–245. https://doi.org/10.1016/S0377-0273(03)00171-9

Bekaert, D. P. S., Walters, R. J., Wright, T. J., Hooper, A. J., & Parker, D. J. (2015). Statistical comparison of InSAR tropospheric correction techniques. *Remote Sensing of Environment*, *170*, 40–47. https://doi.org/10.1016/j.rse.2015.08.035

Berglund, H. T., Sheehan, A. F., Murray, M. H., Roy, M., Lowry, A. R., Nerem, R. S., & Blume, F. (2012). Distributed deformation across the Rio Grande Rift, Great Plains, and Colorado Plateau. *Geology*, *40*(1), 23–26. https://doi.org/10.1130/G32418.1

Block, G. A., Roy, M., Graves, E., & Grapenthin, R. (2023). Pressurizing Magma Within Heterogeneous Crust: A Case Study at the Socorro Magma Body, New Mexico, USA. *Geophysical Research Letters*, *50*(20). https://doi.org/10.1029/2023GL105689

Bock, Y., Nikolaidis, R. M., de Jonge, P. J., & Bevis, M. (2000). Instantaneous geodetic positioning at medium distances with the Global Positioning System. *Journal of Geophysical Research: Solid Earth*, *105*(B12), 28223–28253. https://doi.org/10.1029/2000JB900268

Broxton, D. E., & Vaniman, D. T. (2005). Geologic Framework of a Groundwater System on the Margin of a Rift Basin, Pajarito Plateau, North-Central New Mexico. *Vadose Zone Journal*, *4*(3), 522–550. https://doi.org/10.2136/vzj2004.0073

Coop, J. D., & Givnish, T. J. (2007). Spatial and temporal patterns of recent forest encroachment in montane grasslands of the Valles Caldera, New Mexico, USA. *Journal of Biogeography*, *34*(5), 914–927. https://doi.org/10.1111/j.1365-2699.2006.01660.x

Dixon, T. H., Mao, A., Bursik, M., Heflin, M., Langbein, J., Stein, R., & Webb, F. (1997). Continuous monitoring of surface deformation at Long Valley Caldera, California, with

GPS. *Journal of Geophysical Research: Solid Earth*, *102*(B6), 12017–12034. https://doi.org/10.1029/96JB03902

Dzurisin, D., Lu, Z., Poland, M. P., & Wicks, C. W. (2019). Space-Based Imaging Radar Studies of U.S. Volcanoes. *Frontiers in Earth Science*, *6*. https://doi.org/10.3389/feart.2018.00249

Fialko, Y., & Simons, M. (2001). Evidence for on-going inflation of the Socorro Magma Body, New Mexico, from interferometric synthetic aperture radar imaging. *Geophysical Research Letters*, *28*(18), 3549–3552. https://doi.org/10.1029/2001GL013318

Garthwaite, M. C., Miller, V. L., Saunders, S., Parks, M. M., Hu, G., & Parker, A. L. (2019). A Simplified Approach to Operational InSAR Monitoring of Volcano Deformation in Low- and Middle-Income Countries: Case Study of Rabaul Caldera, Papua New Guinea. *Frontiers in Earth Science*, *6*. https://doi.org/10.3389/feart.2018.00240

Goff, F., and Kelley, S.A., (2021). Facts and hypotheses regarding the ……: New Mexico Geological Society, Guidebook 71, Socorro, p. 101-115.

Goff, F., Gardner, J.N., Reneau, S.L., Kelley, S.A., Kempter, K.A., and Lawrence, J.R., (2011). Geologic map of the Valles caldera, Jemez Mountains, New Mexico: New Mexico Bureau of Geology and Mineral Resources, Geologic Map 79, 1:50,000 scale (color) w/ 30 p. booklet.

Goff, F., & Shevenell, L. (1987). Travertine deposits of Soda Dam, New Mexico, and their implications for the age and evolution of the Valles caldera hydrothermal system. *Geological Society of America Bulletin*, *99*(2), 292. https://doi.org/10.1130/0016-7606(1987)99<292:TDOSDN>2.0.CO;2

Goff, F., Shevenell, L., Gardner, J.N., Vuataz, F.-D., and Grigsby, C.O. (1988). The hydrothermal outflow plume of Valles caldera, New Mexico, and a comparison with other outflow plumes: Journal of Geophysical Research, v. 93, p. 6041-6058.

Havazli, E., & Wdowinski, S. (2021). Detection Threshold Estimates for InSAR Time Series: A Simulation of Tropospheric Delay Approach. *Sensors*, *21*(4), 1124. https://doi.org/10.3390/s21041124

Heiken, G., Goff, F., Gardner, J. N., Baldridge, W. S., Hulen, J. B., Nielson, D. L., & Vaniman, D. (1990). THE VALLES/TOLEDO CALDERA COMPLEX, JEMEZ VOLCANIC FIELD, NEW MEXICO. *Annual Review of Earth and Planetary Sciences*, *18*(1), 27–53. https://doi.org/10.1146/annurev.ea.18.050190.000331

Herring, T. A., King, R. W., & McClusky, S. C. (2018). *GPS analysis at MIT*.

Kelley, S. A., McIntosh, W. C., Goff, F., Kempter, K. A., Wolff, J. A., Esser, R., Braschayko, S., Love, D., & Gardner, J. N. (2013). Spatial and temporal trends in pre-caldera Jemez Mountains volcanic and fault activity. *Geosphere*, *9*(3), 614–646. https://doi.org/10.1130/GES00897.1

Kelley, S.A., McIntosh, W.C., Goff, F., Kempter, K.A., Wolff, J.A., Esser, R., Brascheyko, S., Love, D., and Gardner, J.N., (2013). Spatial and temporal trends in pre-caldera Jemez Mountains and volcanic and fault activity: Geosphere, v. 9, p. 614-646.

Langbein, J. O. (2003). Deformation of the Long Valley Caldera, California: inferences from measurements from 1988 to 2001. *Journal of Volcanology and Geothermal Research*, *127*(3–4), 247–267. https://doi.org/10.1016/S0377-0273(03)00172-0

Liang, C., Agram, P., Simons, M., & Fielding, E. J. (2019). Ionospheric Correction of InSAR Time Series Analysis of C-band Sentinel-1 TOPS Data. *IEEE Transactions on Geoscience and Remote Sensing*, *57*(9), 6755–6773. https://doi.org/10.1109/TGRS.2019.2908494

Massonnet, D., Briole, P., & Arnaud, A. (1995). Deflation of Mount Etna monitored by spaceborne radar interferometry. *Nature*, *375*(6532), 567–570. https://doi.org/10.1038/375567a0

Meister, R., Robertson, E. C., Werre, R. W., & Raspet, R. (1980). Elastic moduli of rock glasses under pressure to 8 kilobars and geophysical implications. *Journal of Geophysical Research: Solid Earth*, *85*(B11), 6461–6470. https://doi.org/10.1029/JB085iB11p06461

Mogi, K., 1958. Relations between the eruptions of various volcanos and the deformation of the ground surfaces around them, Bull. Eurthq. Res. Inst., 36, 99-134.

Murray, K. D., Murray, M. H., & Sheehan, A. F. (2019). Active Deformation Near the Rio Grande Rift and Colorado Plateau as Inferred from Continuous Global Positioning System Measurements. *Journal of Geophysical Research: Solid Earth*, *124*(2), 2166–2183. https://doi.org/10.1029/2018JB016626

Nasholds, M. W. M., & Zimmerer, M. J. (2022). High-precision 40Ar/39Ar geochronology and volumetric investigation of volcanism and resurgence following eruption of the Tshirege Member, Bandelier Tuff, at the Valles caldera. *Journal of Volcanology and Geothermal Research*, *431*, 107624. https://doi.org/10.1016/j.jvolgeores.2022.107624

Palano, M., Calcaterra, S., Gambino, P., Porfidia, B., & Sparacino, F. (2023). GNSS-based long-term deformation at Mount Etna volcano (Italy). *Results in Geophysical Sciences*, *14*, 100056. https://doi.org/10.1016/j.ringps.2023.100056

Perosanz, F. (2019). GNSS: A revolution for precise geopositioning. *Comptes Rendus Physique*, *20*(3), 171–175. https://doi.org/10.1016/j.crhy.2019.05.018

Poland, M. P., & Zebker, H. A. (2022). Volcano geodesy using InSAR in 2020: the past and next decades. *Bulletin of Volcanology*, *84*(3), 27. https://doi.org/10.1007/s00445-022-01531-1

Poland, Michael. https://www.usgs.gov/media/images/deformation-results-pressurization-mogi-source-model.

Reilinger, R. E., & York, J. E. (1979). Relative crystal subsidence from leveling data in a seismically active part of the Rio Grande rift, New Mexico. *Geology*, *7*(3), 139. https://doi.org/10.1130/0091-7613(1979)7<139:RCSFLD>2.0.CO;2

Roberts, P. M., Aki, K., & Fehler, M. C. (1991). A low-velocity zone in the basement beneath the Valles Caldera, New Mexico. *Journal of Geophysical Research: Solid Earth*, *96*(B13), 21583–21596. https://doi.org/10.1029/91JB02048

Rosen, P.A., Gurrola, E, Sacco G.F. and Zebker H. , "The InSAR scientific computing environment," *EUSAR (2012); 9th European Conference on Synthetic Aperture Radar*, Nuremberg, Germany, 2012, pp. 730-733.

Saltogianni, V., & Stiros, S. C. (2013). Topological inversion in geodesy-based, non-linear problems in geophysics. *Computers & Geosciences*, *52*, 379–388. https://doi.org/10.1016/j.cageo.2012.11.010

Silverii, F., Pulvirenti, F., Montgomery-Brown, E. K., Borsa, A. A., & Neely, W. R. (2021). The 2011-2019 Long Valley Caldera inflation: New insights from separation of superimposed geodetic signals and 3D modeling. *Earth and Planetary Science Letters*, *569*, 117055. https://doi.org/10.1016/j.epsl.2021.117055

Suhr, G., 1981, Seismic crust anomaly under the Valles caldera in New Mexico, USA: Unpublished consultant report, PRAKLA-SEISMOS GMBH, Hanover, Federal Republic of Germany, 56 p.

Taylor, N. C., Johnson, J. H., & Herd, R. A. (2021). Making the most of the Mogi model: Size matters. *Journal of Volcanology and Geothermal Research*, *419*, 107380. https://doi.org/10.1016/j.jvolgeores.2021.107380

Tizzani, P., Berardino, P., Casu, F., Euillades, P., Manzo, M., Ricciardi, G., Zeni, G., & Lanari, R. (2007). Surface deformation of Long Valley caldera and Mono Basin, California, investigated with the SBAS-InSAR approach. *Remote Sensing of Environment*, *108*(3), 277–289. https://doi.org/10.1016/j.rse.2006.11.015

Treuhaft, R. N., Madsen, S. N., Moghaddam, M., & van Zyl, J. J. (1996). Vegetation characteristics and underlying topography from interferometric radar. *Radio Science*, *31*(6), 1449–1485. https://doi.org/10.1029/96RS01763

van Wijk, J., Koning, D., Axen, G., Coblentz, D., Gragg, E., & Sion, B. (2018). Tectonic subsidence, geoid analysis, and the Miocene-Pliocene unconformity in the Rio Grande rift, southwestern United States: Implications for mantle upwelling as a driving force for rift opening. *Geosphere*, *14*(2), 684–709. https://doi.org/10.1130/GES01522.1

Vasco, D. W., Puskas, C. M., Smith, R. B., & Meertens, C. M. (2007). Crustal deformation and source models of the Yellowstone volcanic field from geodetic data. *Journal of Geophysical Research: Solid Earth*, *112*(B7). https://doi.org/10.1029/2006JB004641

Wang, G., & Li, S. F. (2004). A penny-shaped cohesive crack model for material damage. *Theoretical and Applied Fracture Mechanics*, *42*(3), 303–316. https://doi.org/10.1016/j.tafmec.2004.09.005

Wannamaker, P. E. (1997). Tensor CSAMT survey over the Sulphur Springs thermal area, Valles Caldera, New Mexico, United States of America, Part I: Implications for structure of the western caldera. *GEOPHYSICS*, *62*(2), 451–465. https://doi.org/10.1190/1.1444156

Webb, F. H., Bursik, M., Dixon, T., Farina, F., Marshall, G., & Stein, R. S. (1995). Inflation of Long Valley Caldera from one year of continuous GPS observations. *Geophysical Research Letters*, *22*(3), 195–198. https://doi.org/10.1029/94GL02968

Wilgus, J., Schmandt, B., Maguire, R., Jiang, C., & Chaput, J. (2023). Shear Velocity Evidence of Upper Crustal Magma Storage Beneath Valles Caldera. *Geophysical Research Letters*, *50*(5). https://doi.org/10.1029/2022GL101520

Wolff, J. A., Brunstad, K. A., & Gardner, J. N. (2011). Reconstruction of the most recent volcanic eruptions from the Valles caldera, New Mexico. *Journal of Volcanology and Geothermal Research*, *199*(1–2), 53–68. https://doi.org/10.1016/j.jvolgeores.2010.10.008

Wolff, J. A., & Gardner, J. N. (1995). Is the Valles caldera entering a new cycle of activity? *Geology*, *23*(5), 411. https://doi.org/10.1130/0091-7613(1995)023<0411:ITVCEA>2.3.CO;2

Wright, T. J., Parsons, B. E., & Lu, Z. (2004). Toward mapping surface deformation in three dimensions using InSAR. *Geophysical Research Letters*, *31*(1). https://doi.org/10.1029/2003GL018827

Zimmerer, M. J., Lafferty, J., & Coble, M. A. (2016). The eruptive and magmatic history of the youngest pulse of volcanism at the Valles caldera: Implications for successfully dating late Quaternary eruptions. *Journal of Volcanology and Geothermal Research*, *310*, 50–57. https://doi.org/10.1016/j.jvolgeores.2015.11.021

Yunjun, Z., Fattahi, H., & Amelung, F. (2019). Small baseline InSAR time series analysis: Unwrapping error correction and noise reduction. *Computers & Geosciences*, *133*, 104331. https://doi.org/10.1016/j.cageo.2019.104331

LIST OF APPENDICIES

APPENDIX 1

APPENDIX 1

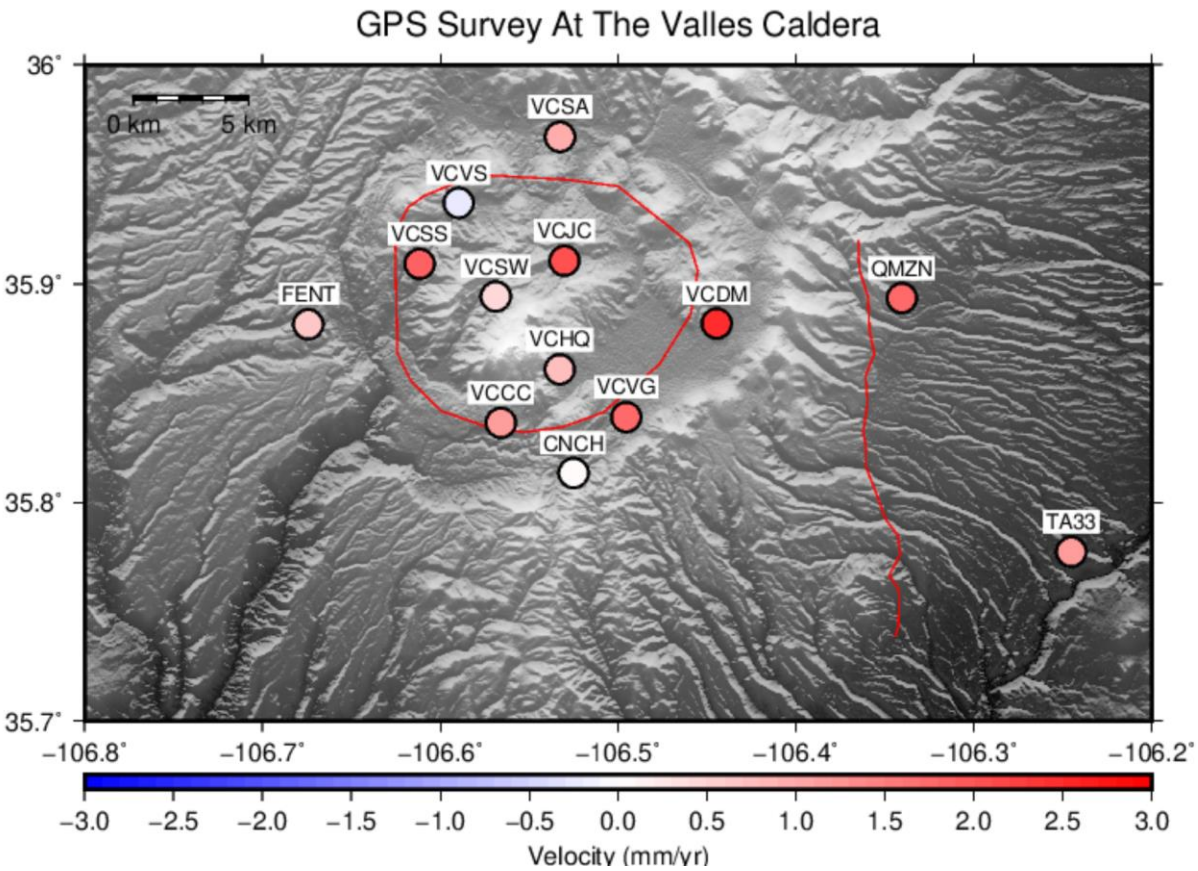

Figure A1. The 13 GPS stations processed from 2002-2022 with the GLOBK-calculated velocities indicated. The average velocity (vertical deformation) is 0.06 mm/yr. These velocities are in relation to station CNCH (indicated on Figure 18). The magnitude of the majority of these stations is less than the average GLOBK-calculated error, which is ±0.43 mm/yr.

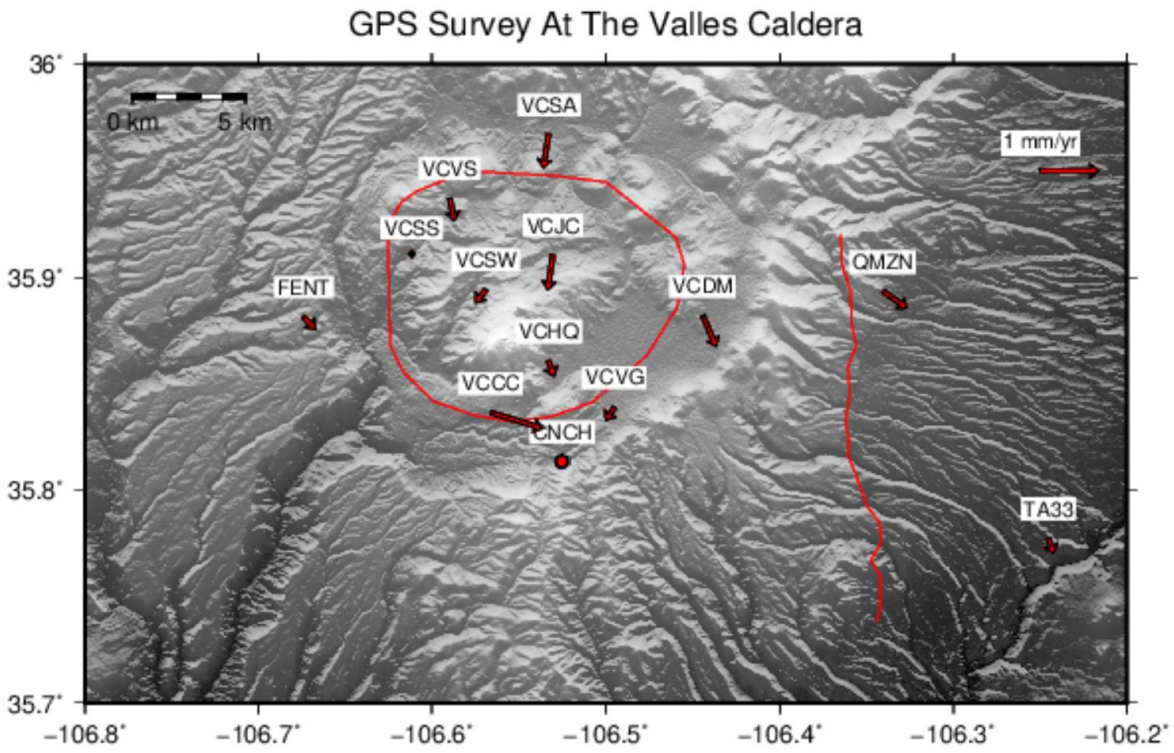

Figure A2. The 13 GPS stations processed from 2002-2022 with the GLOBK-calculated horizontal velocities indicated. The average horizontal motion is 1.13 mm/yr to the south and 0.1 mm/yr to the west. The arrow labeled “1 mm/yr” is for scale. These velocities are in relation to station CNCH (indicated on Figure 18).

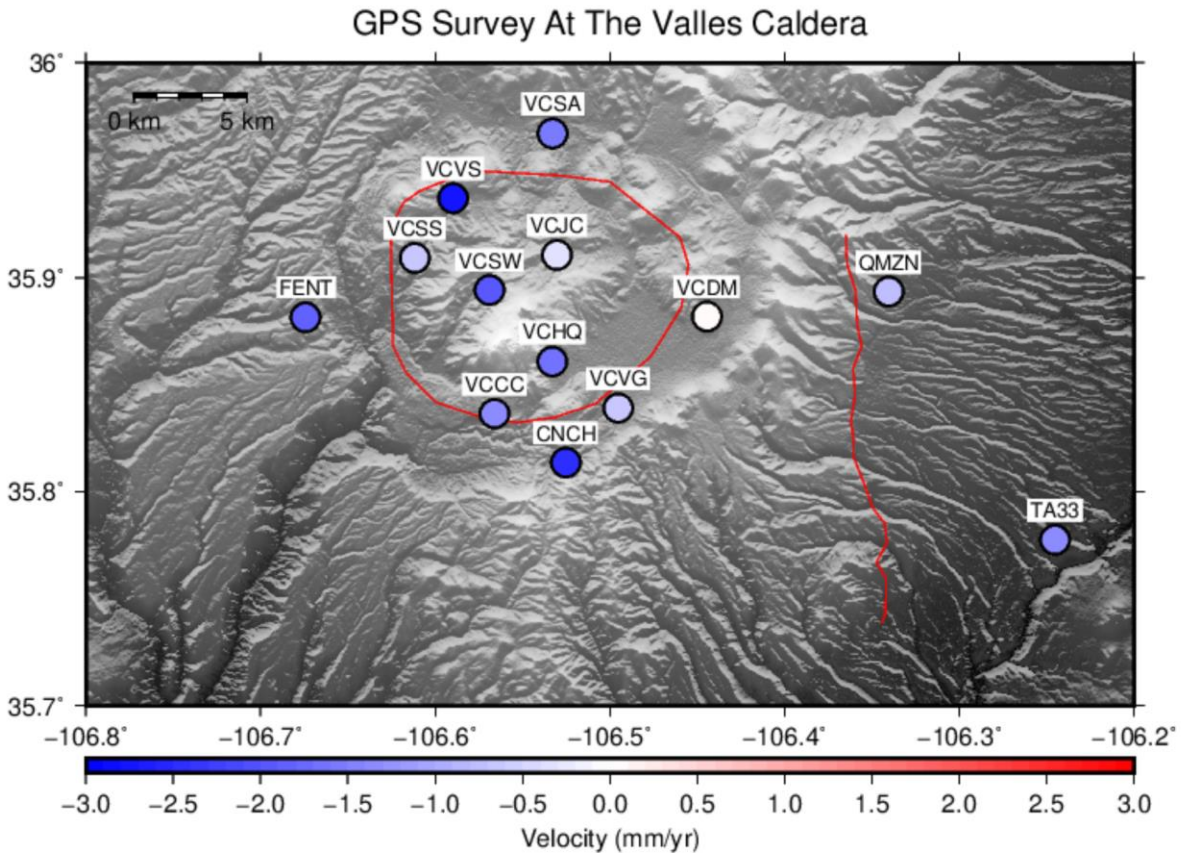

Figure A3. The 13 GPS stations processed from 2002-2022 with the GLOBK-calculated velocities indicated. The average velocity (vertical deformation) is 0.06 mm/yr. These velocities are in relation to station VCDM (indicated on Figure 18). The magnitude of the majority of these stations is less than the average GLOBK-calculated error, which is ±0.43 mm/yr.

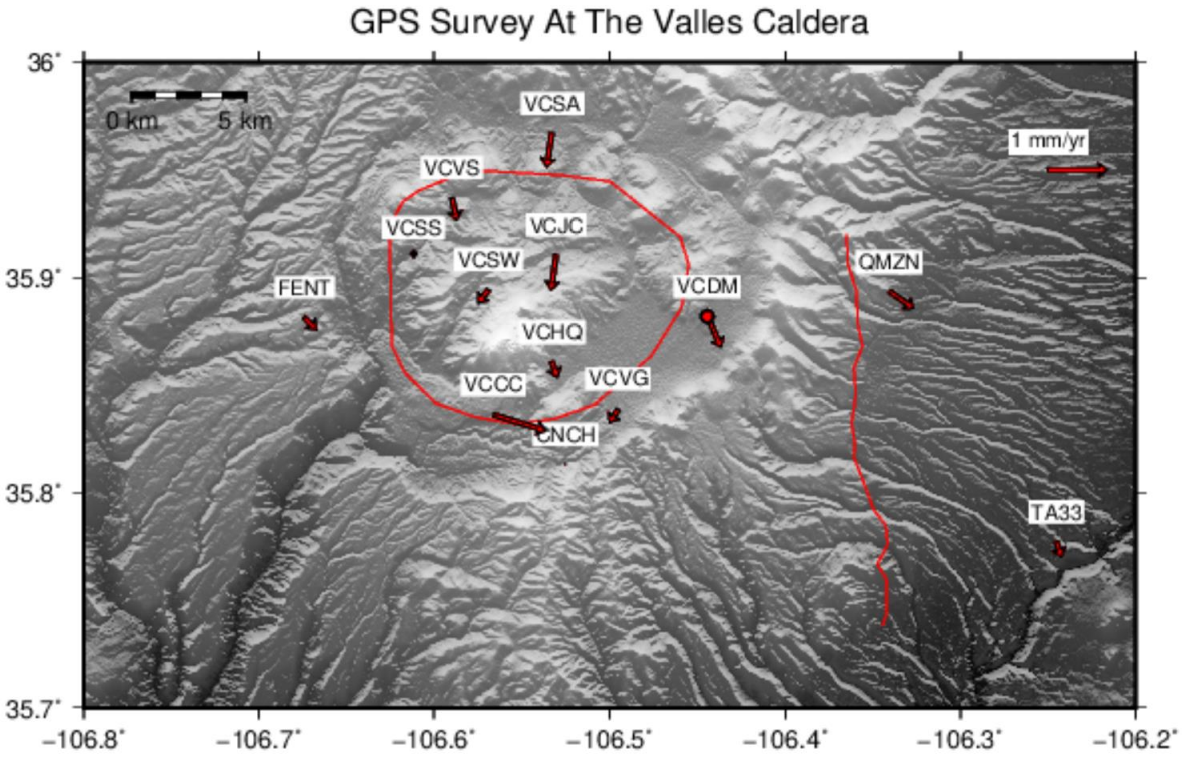

Figure A4. The 13 GPS stations processed from 2002-2022 with the GLOBK-calculated horizontal velocities indicated. The average horizontal motion is 1.13 mm/yr to the south and 0.1 mm/yr to the west. The arrow labeled “1 mm/yr” is for scale. These velocities are in relation to station VCDM (indicated on Figure 18).

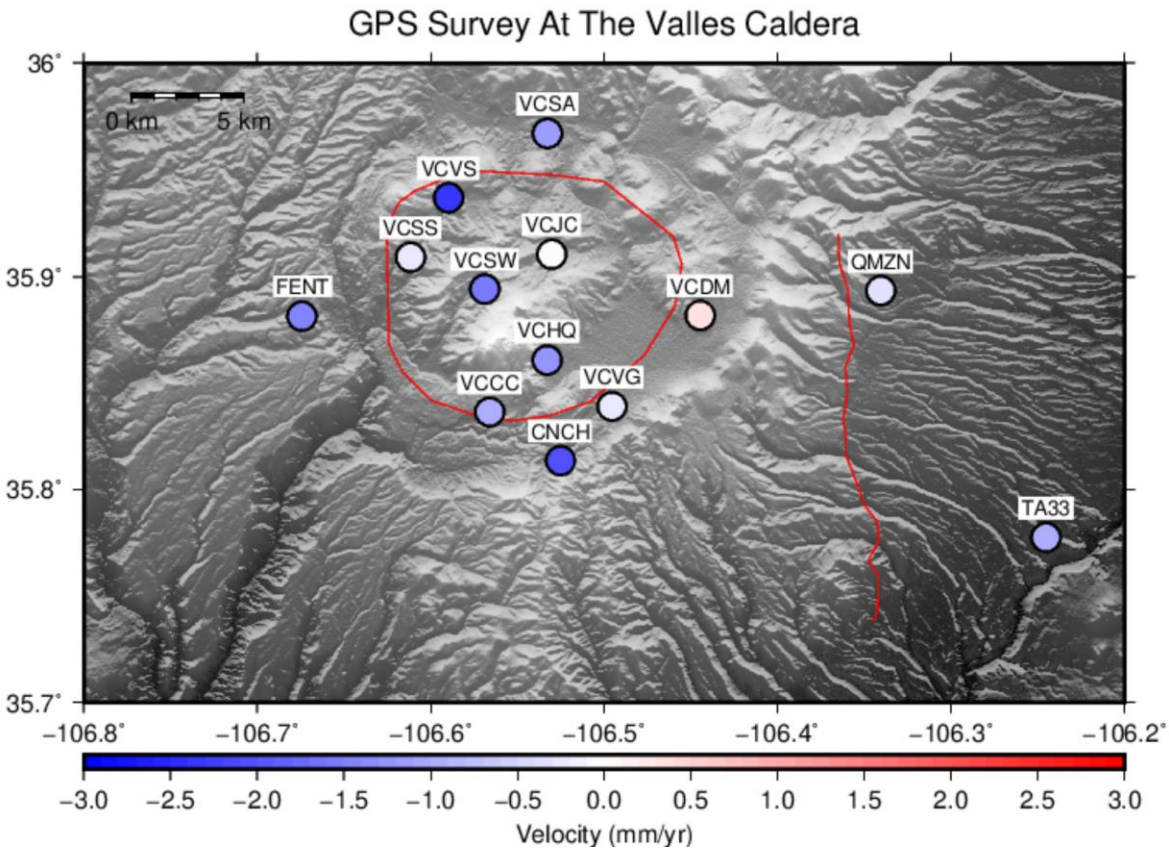

Figure A5. The 13 GPS stations processed from 2002-2022 with the GLOBK-calculated velocities indicated. The average velocity (vertical deformation) is 0.06 mm/yr. These velocities are in relation to station VCJC (indicated on Figure 18). The magnitude of the majority of these stations is less than the average GLOBK-calculated error, which is ±0.43 mm/yr.

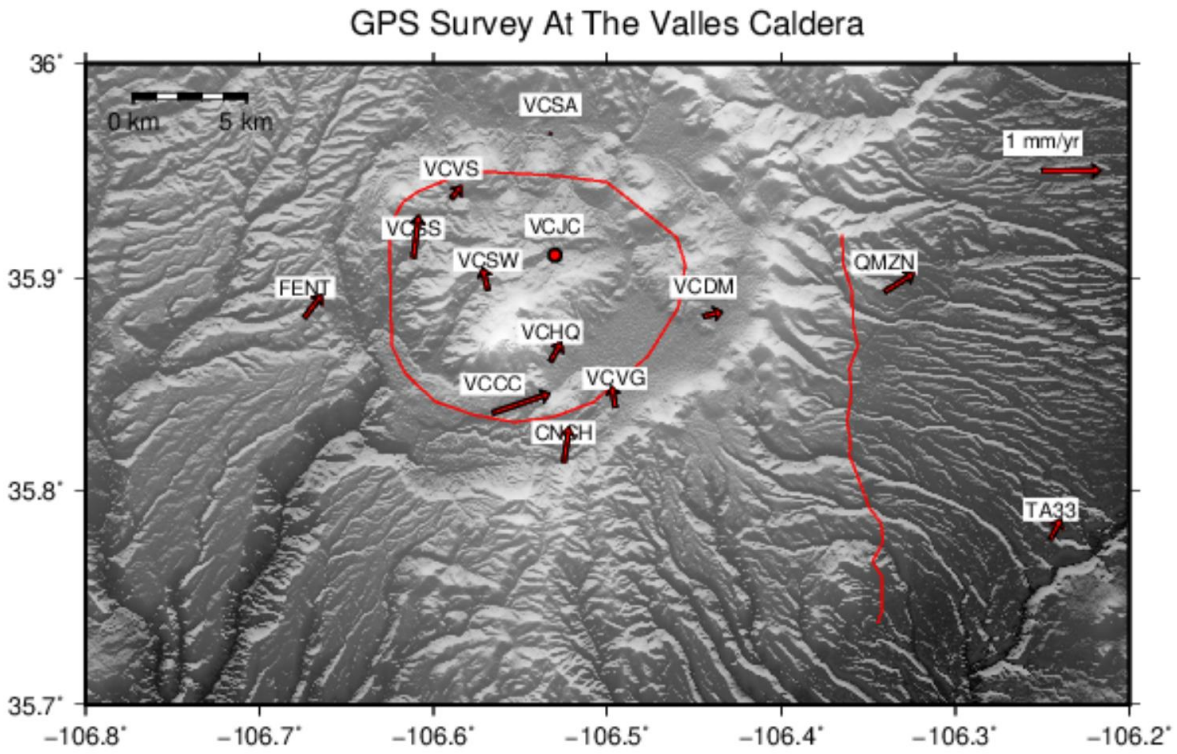

Figure A6. The 13 GPS stations processed from 2002-2022 with the GLOBK-calculated horizontal velocities indicated. The average horizontal motion is 1.13 mm/yr to the south and 0.1 mm/yr to the west. The arrow labeled “1 mm/yr” is for scale. These velocities are in relation to station VCJC (indicated on Figure 18).

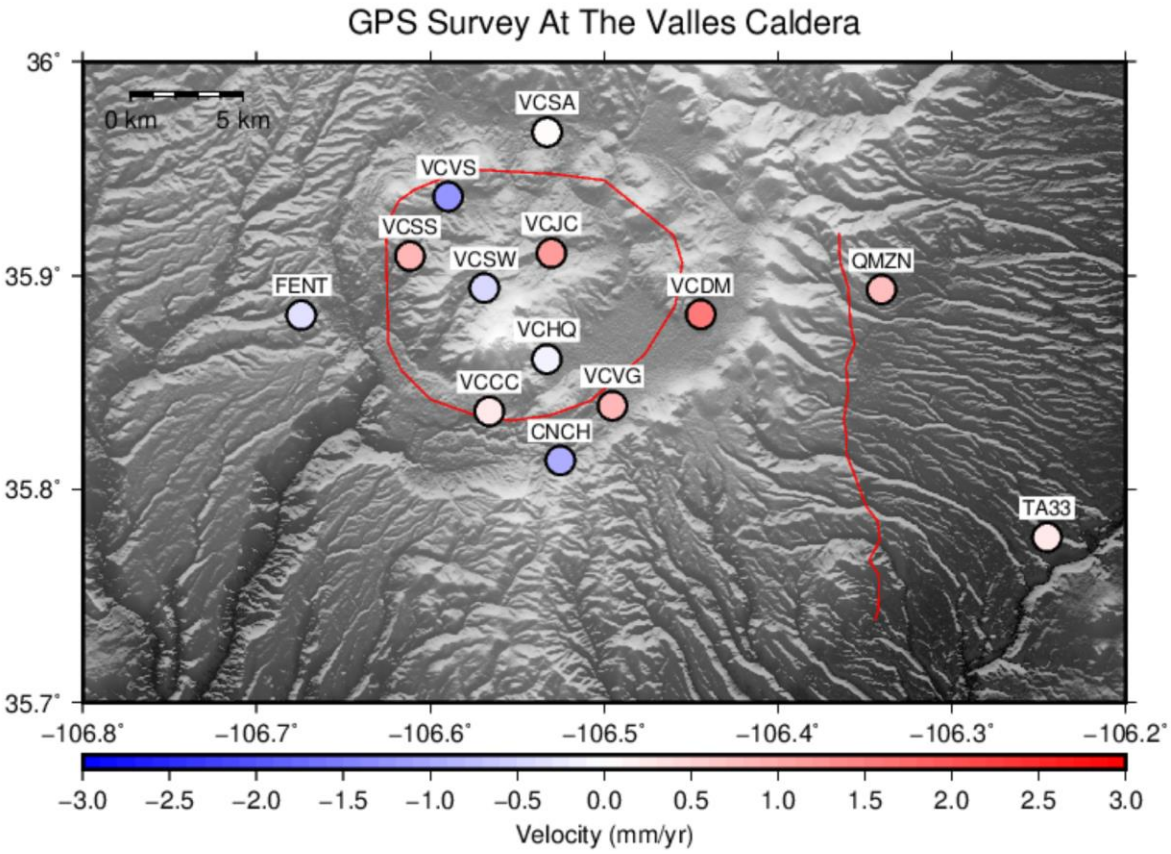

Figure A7. The 13 GPS stations processed from 2002-2022 with the GLOBK-calculated velocities indicated. The average velocity (vertical deformation) is 0.06 mm/yr. These velocities are in relation to station VCSA (indicated on Figure 18). The magnitude of the majority of these stations is less than the average GLOBK-calculated error, which is ±0.43 mm/yr.

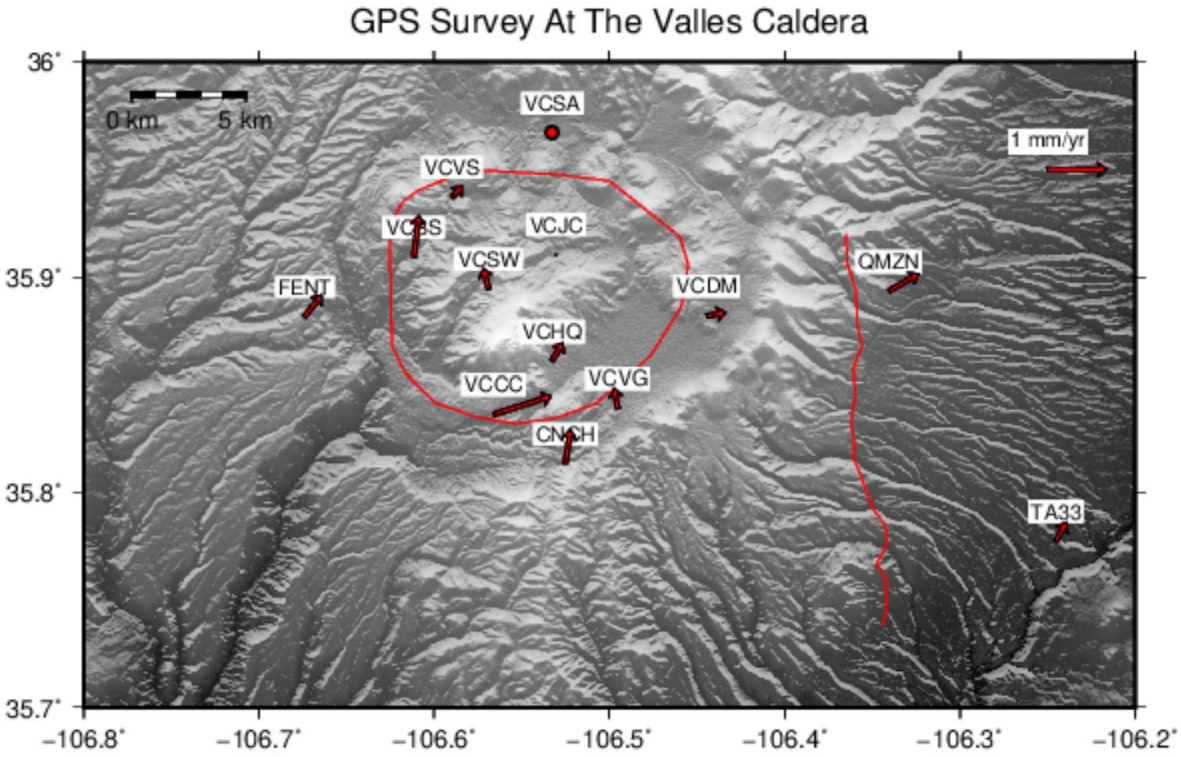

Figure A8. The 13 GPS stations processed from 2002-2022 with the GLOBK-calculated horizontal velocities indicated. The average horizontal motion is 1.13 mm/yr to the south and 0.1 mm/yr to the west. The arrow labeled “1 mm/yr” is for scale. These velocities are in relation to station VCSA (indicated on Figure 18).

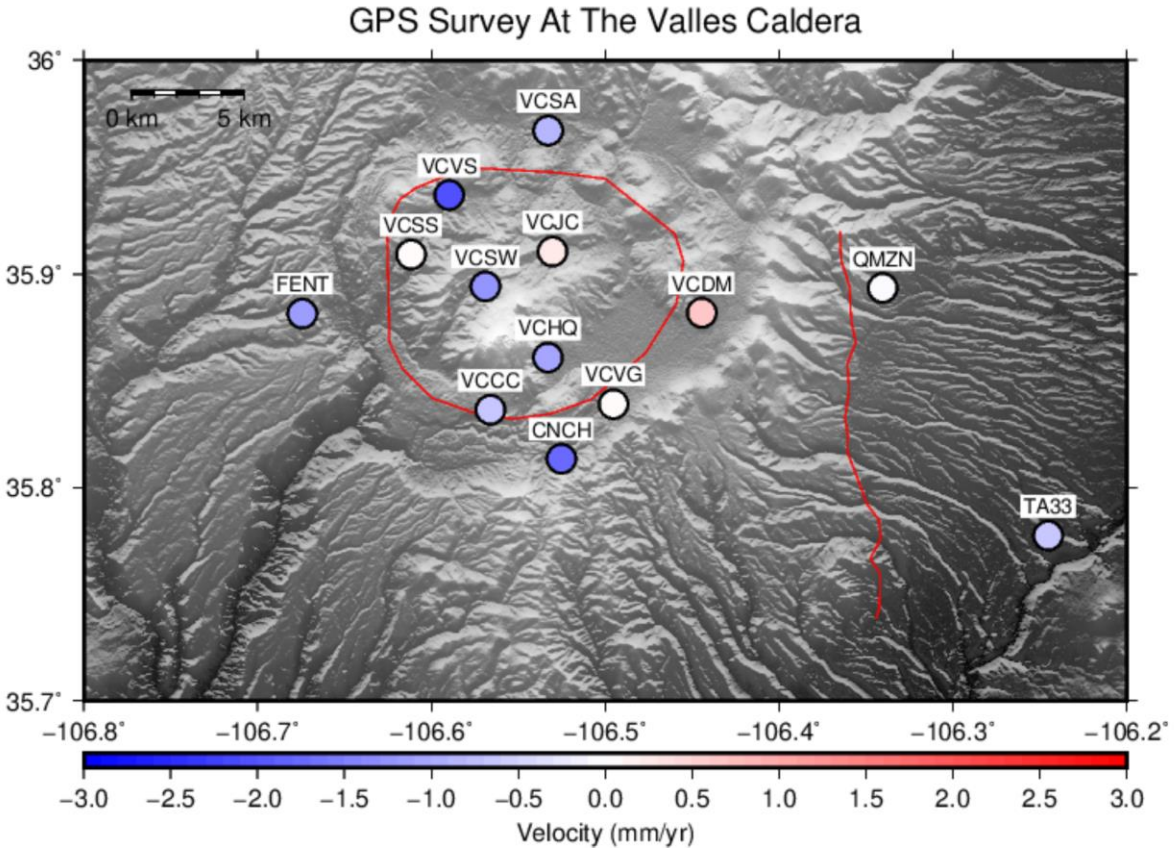

Figure A9. The 13 GPS stations processed from 2002-2022 with the GLOBK-calculated velocities indicated. The average velocity (vertical deformation) is 0.06 mm/yr. These velocities are in relation to station VCVG (indicated on Figure 18). The magnitude of the majority of these stations is less than the average GLOBK-calculated error, which is ±0.43 mm/yr.

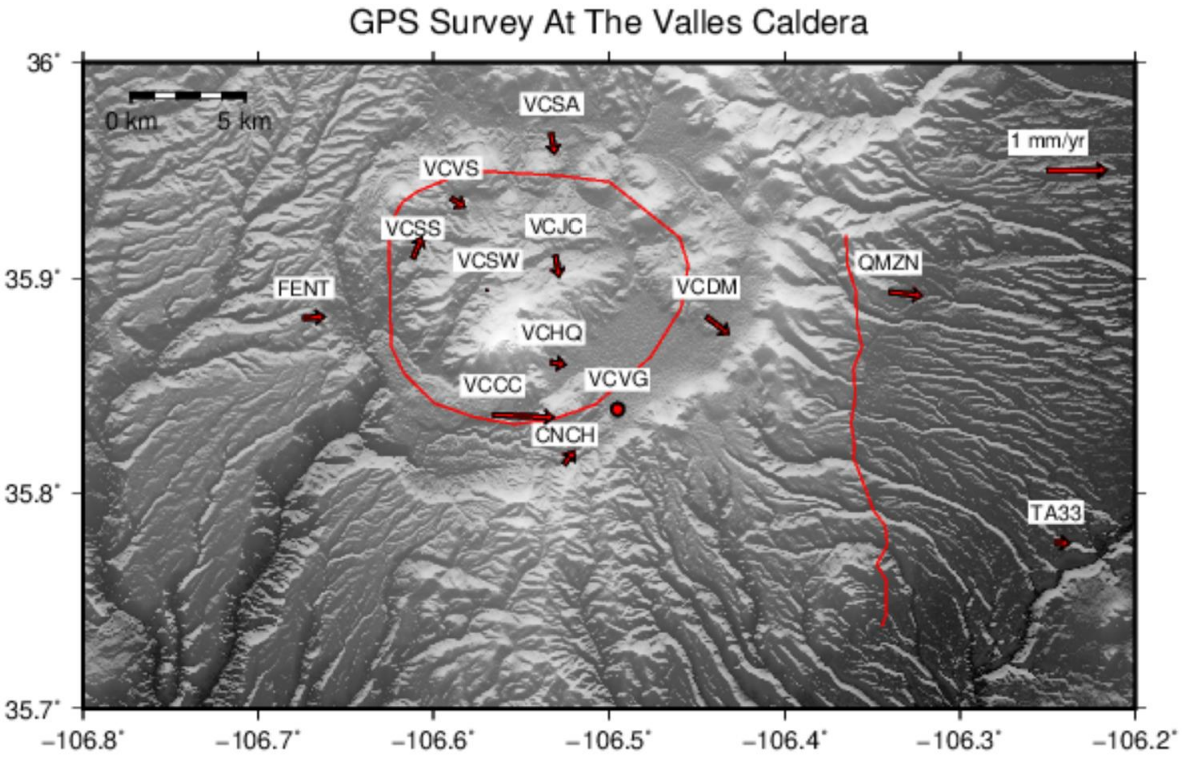

Figure A10. The 13 GPS stations processed from 2002-2022 with the GLOBK-calculated horizontal velocities indicated. The average horizontal motion is 1.13 mm/yr to the south and 0.1 mm/yr to the west. The arrow labeled “1 mm/yr” is for scale. These velocities are in relation to station VCVG (indicated on Figure 18).

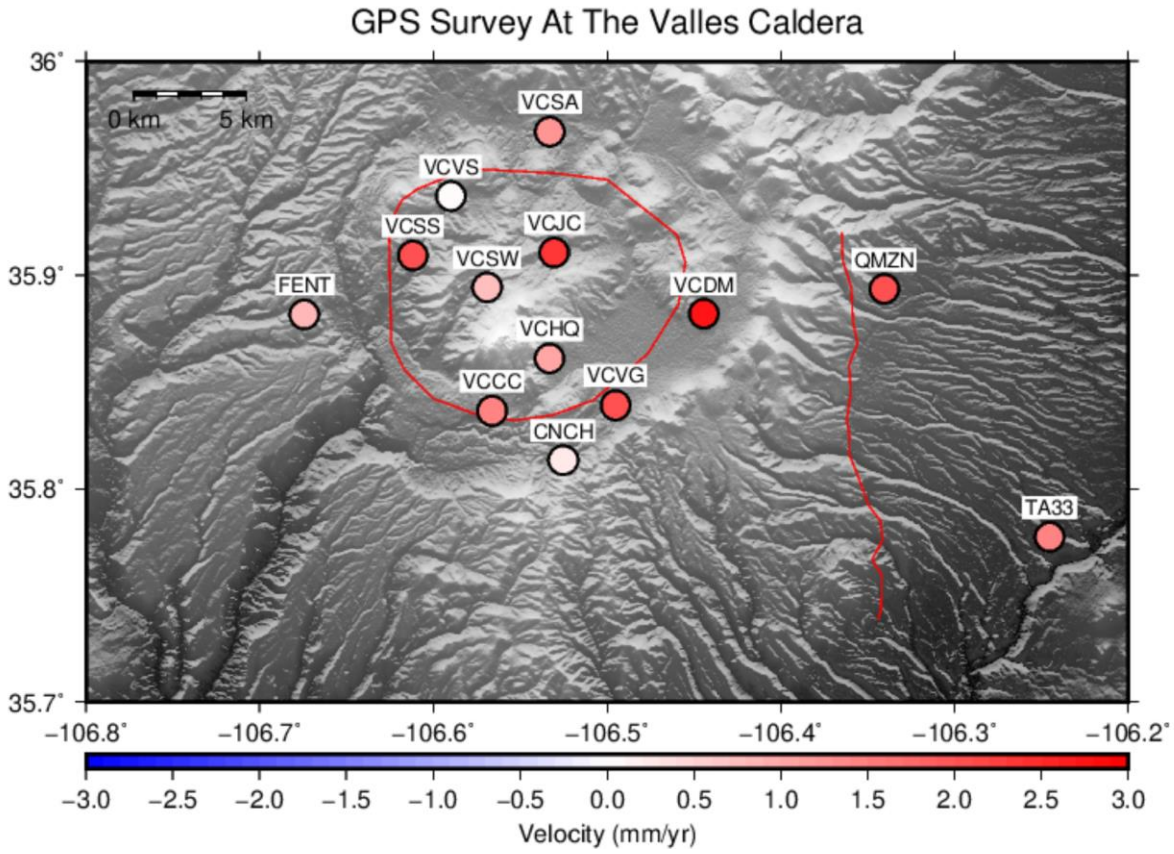

Figure A11. The 13 GPS stations processed from 2002-2022 with the GLOBK-calculated velocities indicated. The average velocity (vertical deformation) is 0.06 mm/yr. These velocities are in relation to station VCVS (indicated on Figure 18). The magnitude of the majority of these stations is less than the average GLOBK-calculated error, which is ±0.43 mm/yr.

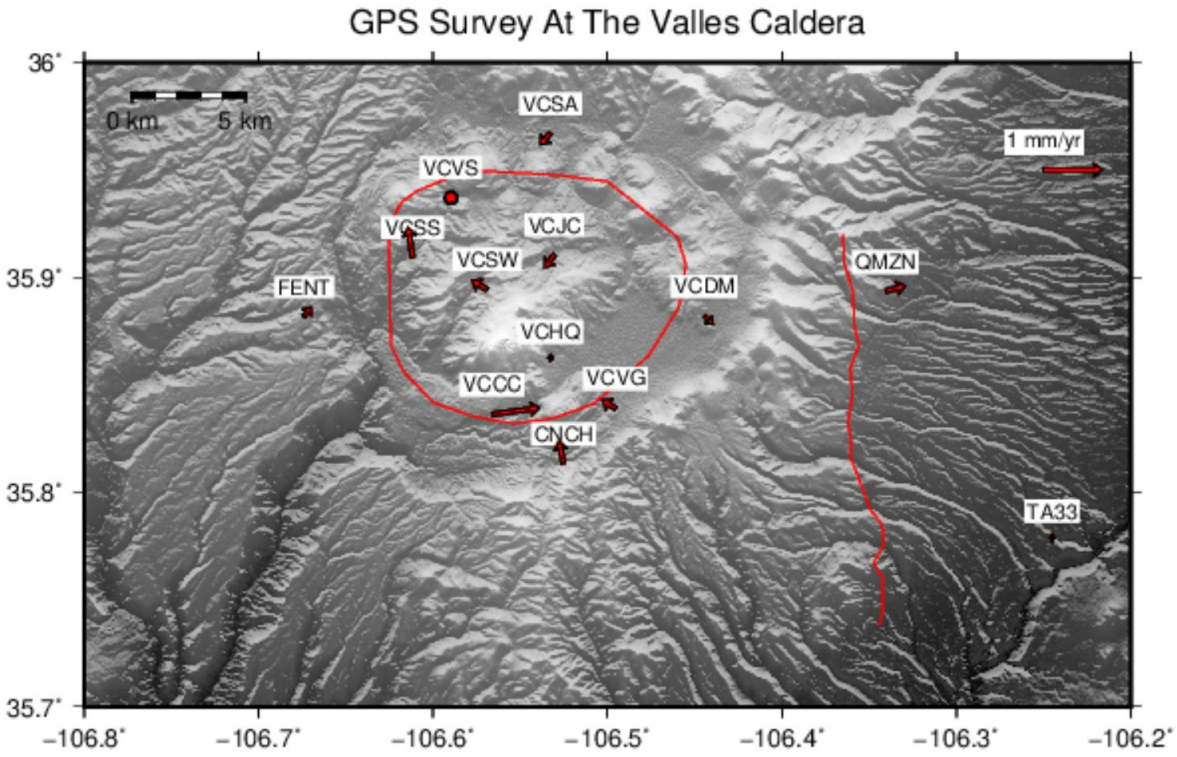

Figure A12. The 13 GPS stations processed from 2002-2022 with the GLOBK-calculated horizontal velocities indicated. The average horizontal motion is 1.13 mm/yr to the south and 0.1 mm/yr to the west. The arrow labeled “1 mm/yr” is for scale. These velocities are in relation to station VCVS (indicated on Figure 18).

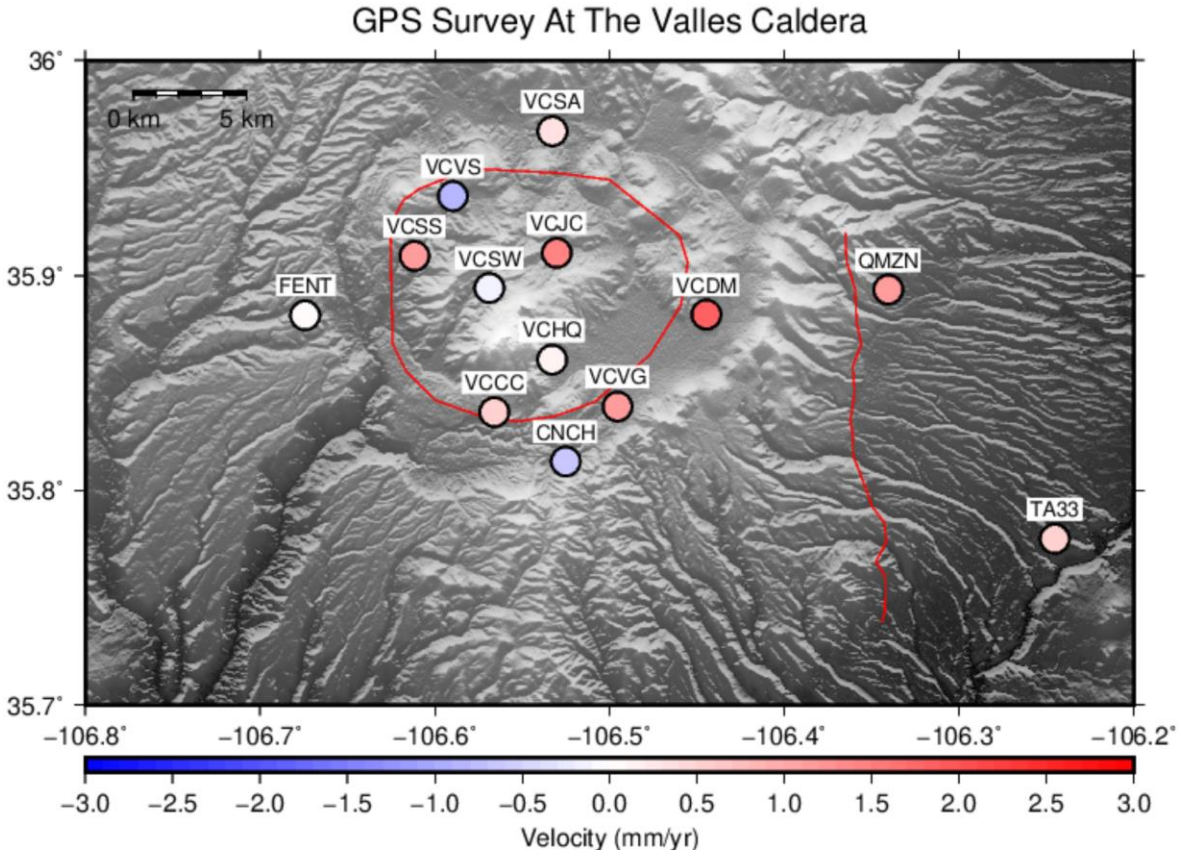

Figure A13. The 13 GPS stations processed from 2002-2022 with the GLOBK-calculated velocities indicated. The average velocity (vertical deformation) is 0.06 mm/yr. These velocities are in relation to station FENT (indicated on Figure 18). The magnitude of the majority of these stations is less than the average GLOBK-calculated error, which is ±0.43 mm/yr.

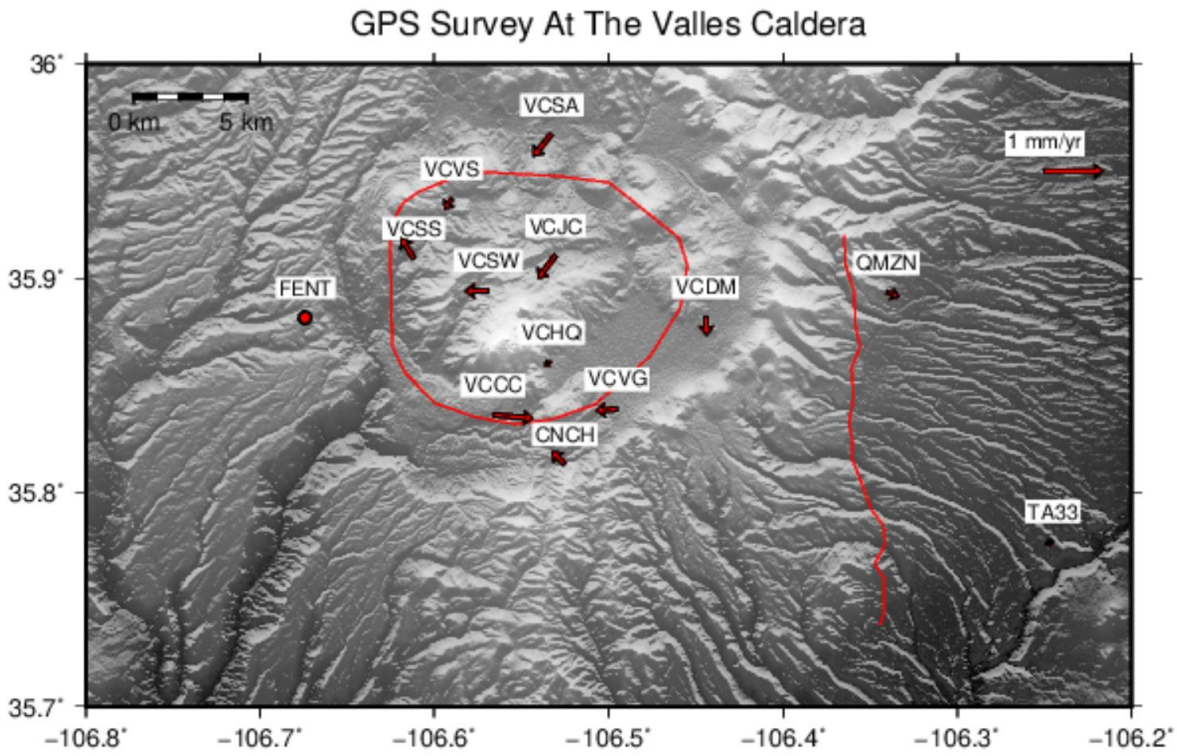

Figure A14. The 13 GPS stations processed from 2002-2022 with the GLOBK-calculated horizontal velocities indicated. The average horizontal motion is 1.13 mm/yr to the south and 0.1 mm/yr to the west. The arrow labeled “1 mm/yr” is for scale. These velocities are in relation to station FENT (indicated on Figure 18).

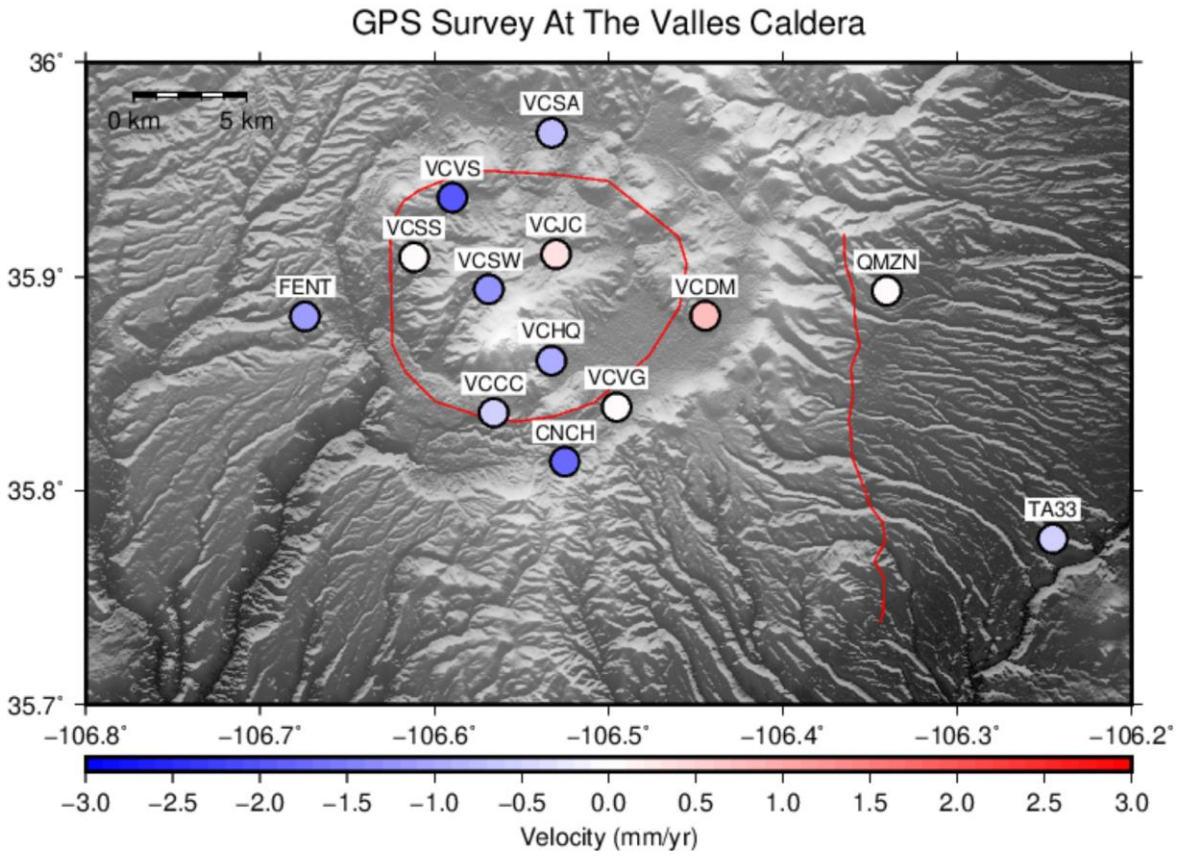

Figure A15. The 13 GPS stations processed from 2002-2022 with the GLOBK-calculated velocities indicated. The average velocity (vertical deformation) is 0.06 mm/yr. These velocities are in relation to station QMZN (indicated on Figure 18). The magnitude of the majority of these stations is less than the average GLOBK-calculated error, which is ±0.43 mm/yr.

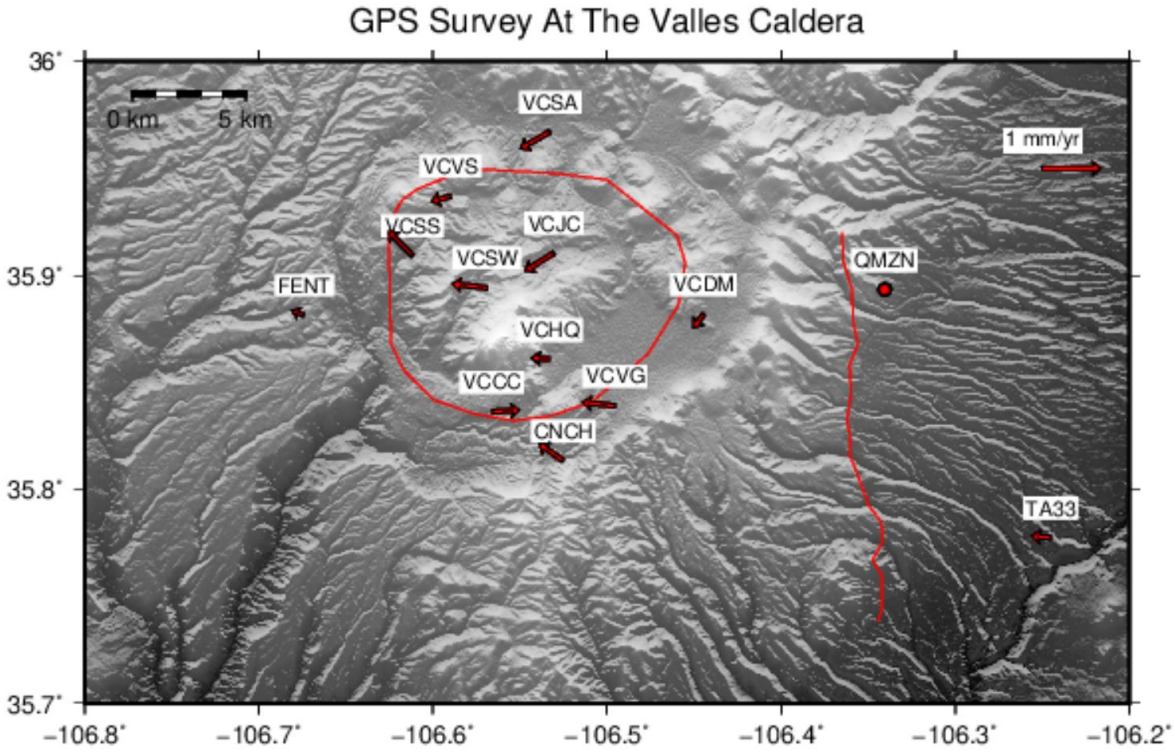

Figure A16. The 13 GPS stations processed from 2002-2022 with the GLOBK-calculated horizontal velocities indicated. The average horizontal motion is 1.13 mm/yr to the south and 0.1 mm/yr to the west. The arrow labeled “1 mm/yr” is for scale. These velocities are in relation to station QMZN (indicated on Figure 18).

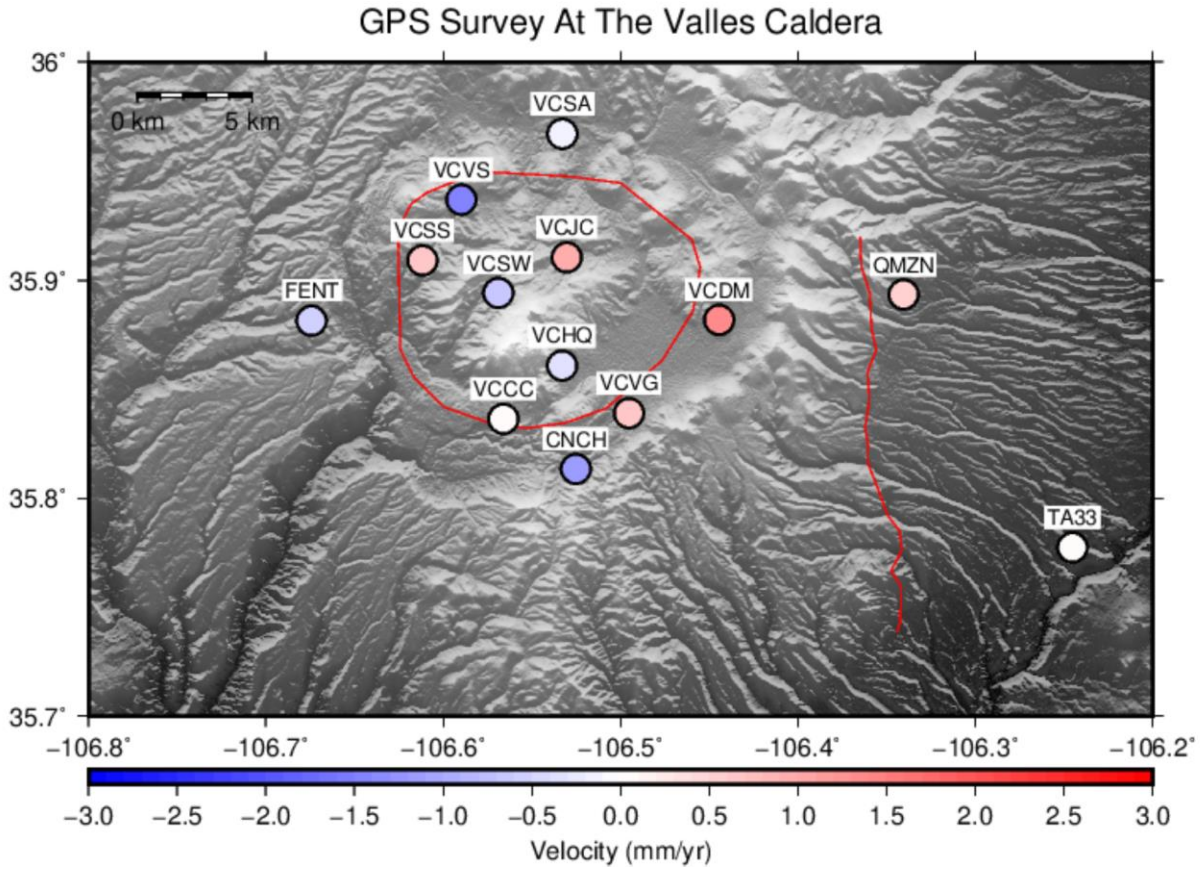

Figure A17. The 13 GPS stations processed from 2002-2022 with the GLOBK-calculated velocities indicated. The average velocity (vertical deformation) is 0.06 mm/yr. These velocities are in relation to station VCCC (indicated on Figure 18). The magnitude of the majority of these stations is less than the average GLOBK-calculated error, which is ±0.43 mm/yr.

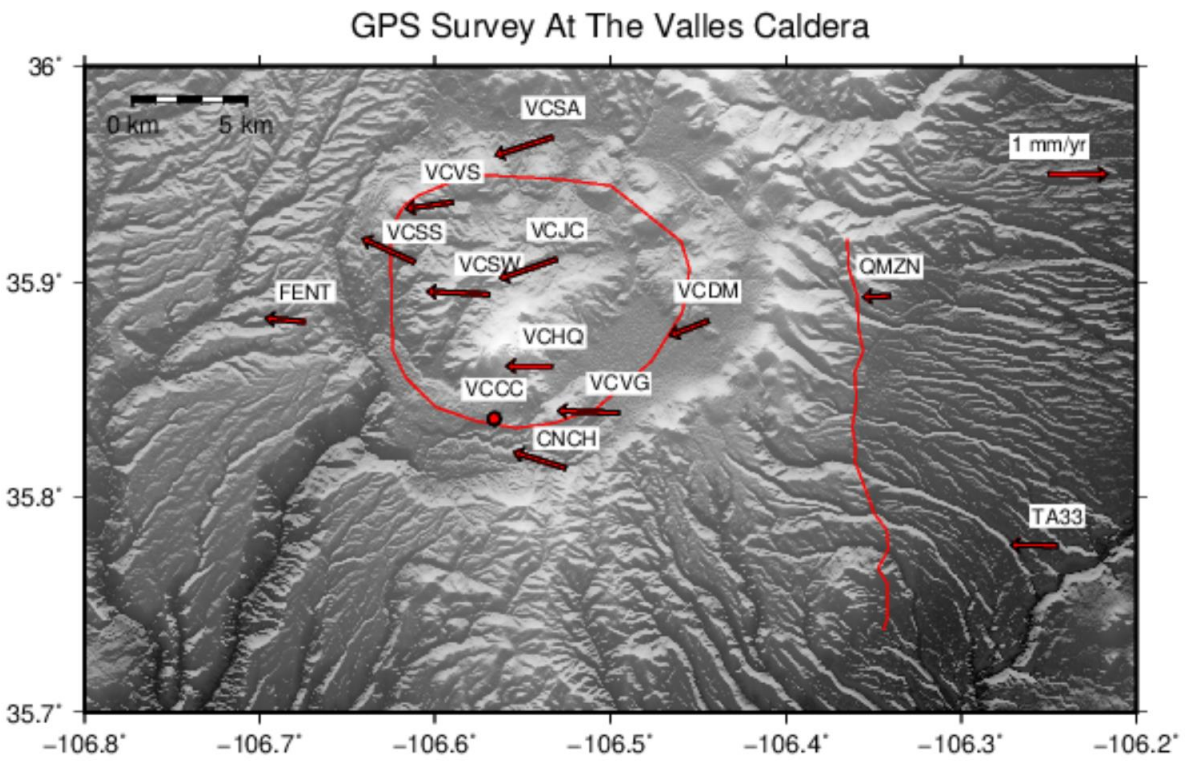

Figure A18. The 13 GPS stations processed from 2002-2022 with the GLOBK-calculated horizontal velocities indicated. The average horizontal motion is 1.13 mm/yr to the south and 0.1 mm/yr to the west. The arrow labeled “1 mm/yr” is for scale. These velocities are in relation to station VCCC (indicated on Figure 18).

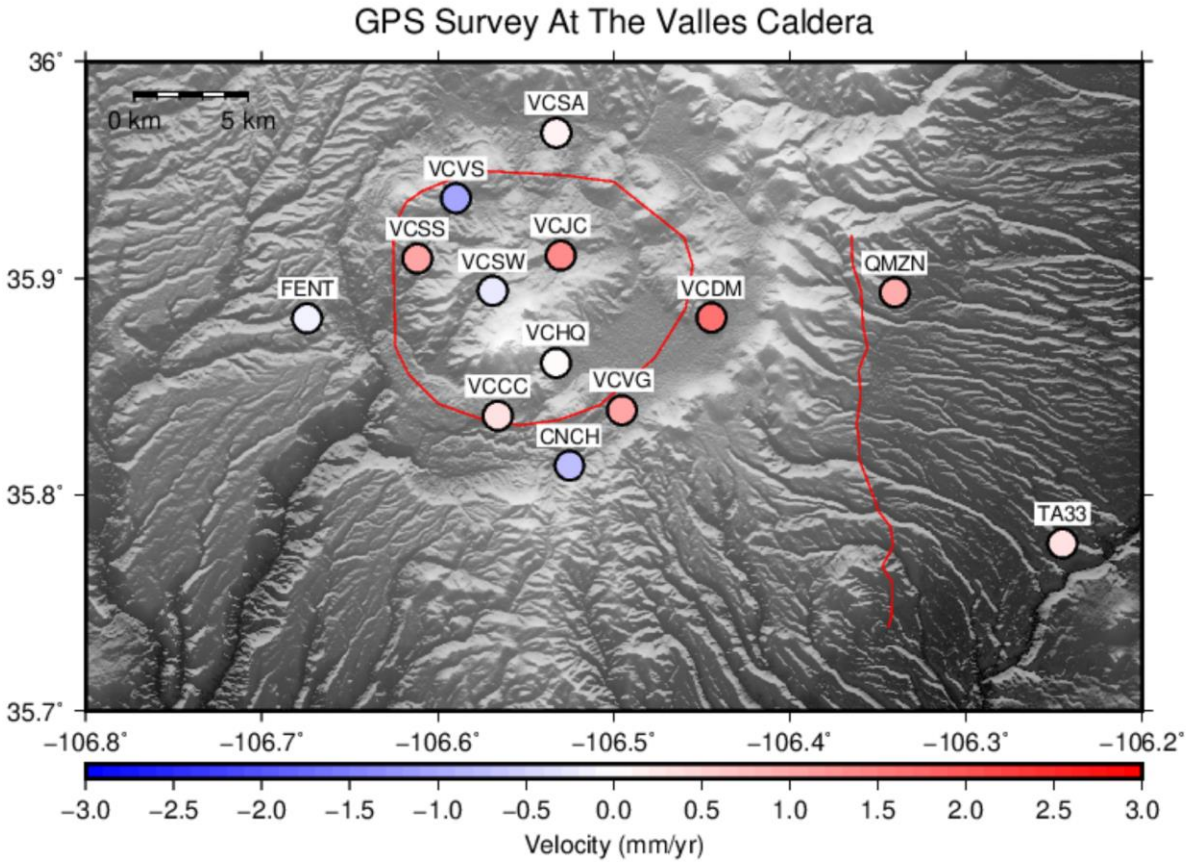

Figure A19. The 13 GPS stations processed from 2002-2022 with the GLOBK-calculated velocities indicated. The average velocity (vertical deformation) is 0.06 mm/yr. These velocities are in relation to station VCHQ (indicated on Figure 18). The magnitude of the majority of these stations is less than the average GLOBK-calculated error, which is ±0.43 mm/yr.

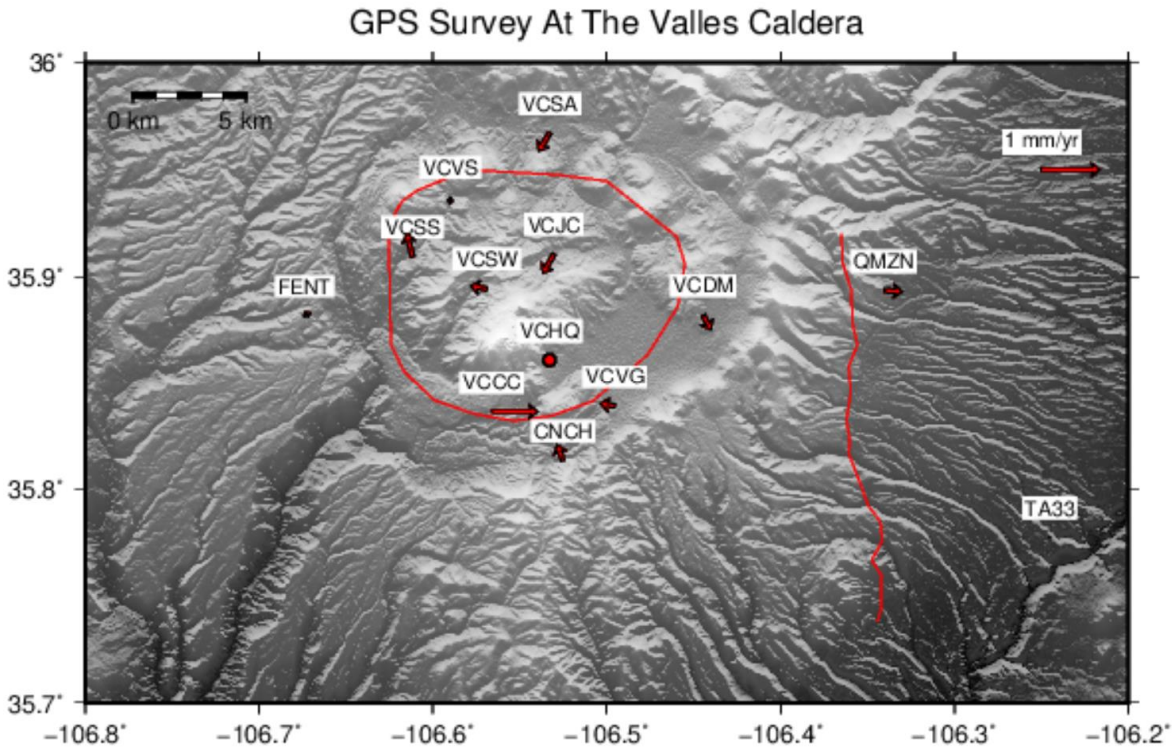

Figure A20. The 13 GPS stations processed from 2002-2022 with the GLOBK-calculated horizontal velocities indicated. The average horizontal motion is 1.13 mm/yr to the south and 0.1 mm/yr to the west. The arrow labeled “1 mm/yr” is for scale. These velocities are in relation to station VCHQ (indicated on Figure 18).

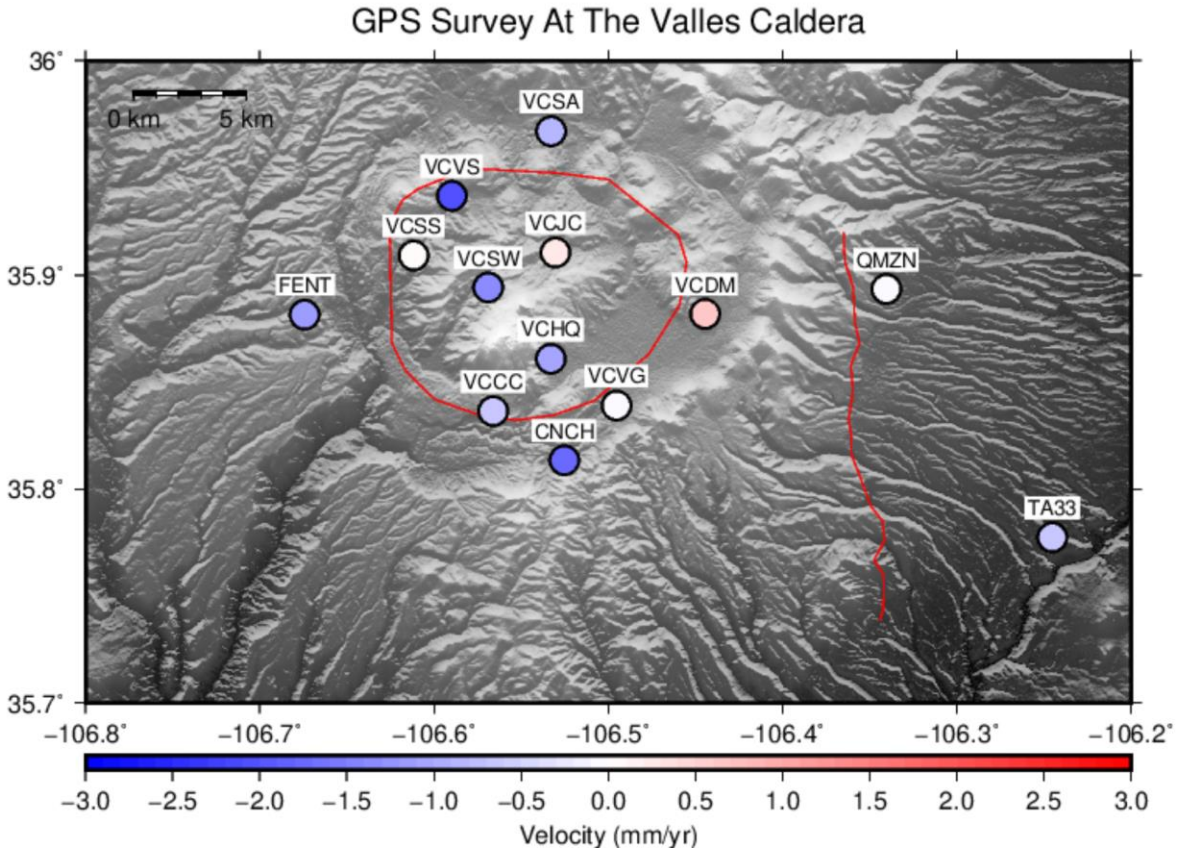

Figure A21. The 13 GPS stations processed from 2002-2022 with the GLOBK-calculated velocities indicated. The average velocity (vertical deformation) is 0.06 mm/yr. These velocities are in relation to station VCSS (indicated on Figure 18). The magnitude of the majority of these stations is less than the average GLOBK-calculated error, which is ±0.43 mm/yr.

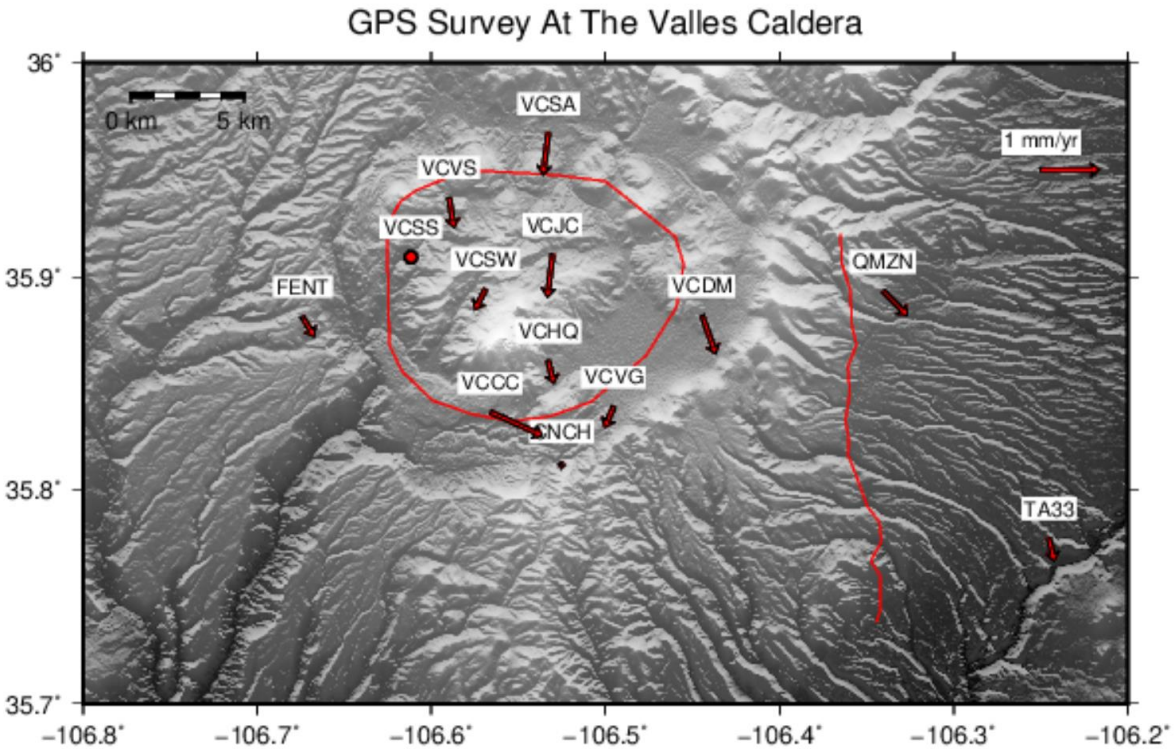

Figure A22. The 13 GPS stations processed from 2002-2022 with the GLOBK-calculated horizontal velocities indicated. The average horizontal motion is 1.13 mm/yr to the south and 0.1 mm/yr to the west. The arrow labeled “1 mm/yr” is for scale. These velocities are in relation to station VCSS (indicated on Figure 18).

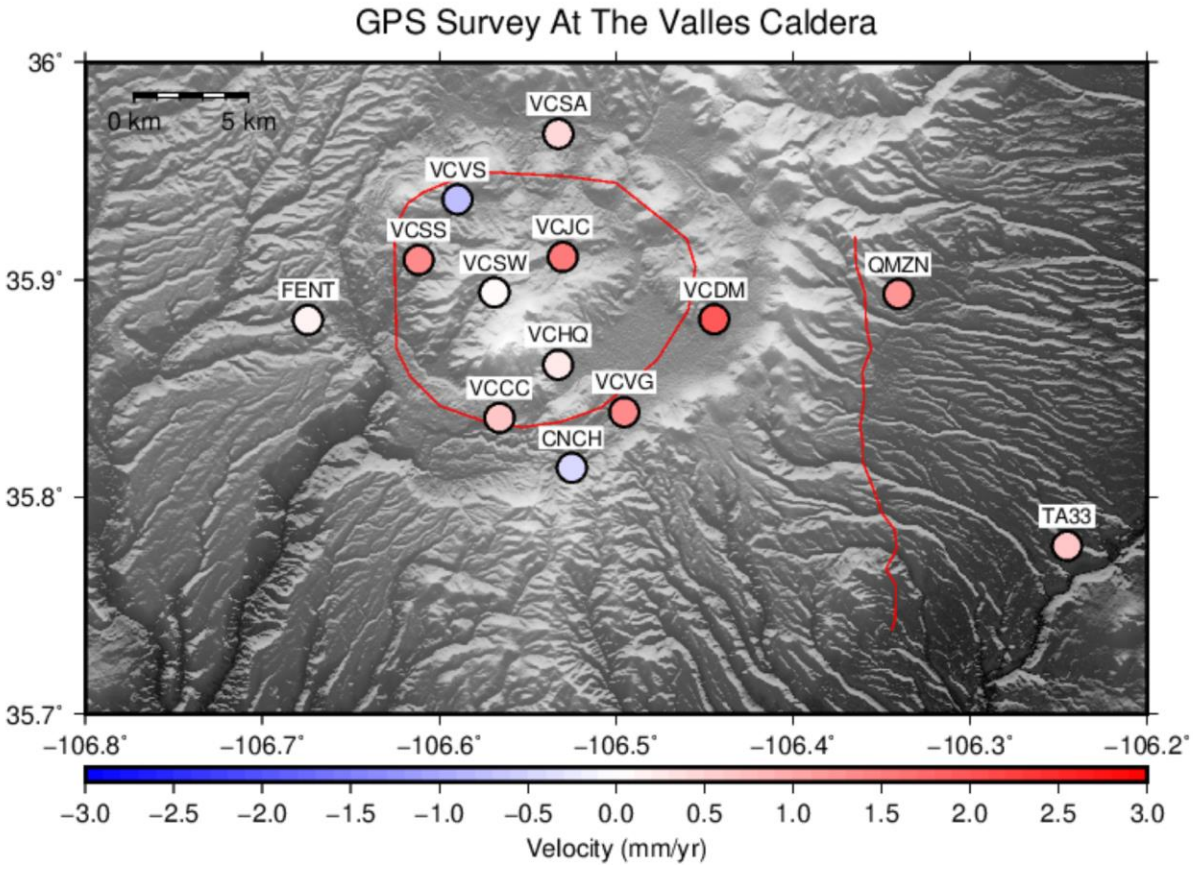

Figure A23. The 13 GPS stations processed from 2002-2022 with the GLOBK-calculated velocities indicated. The average velocity (vertical deformation) is 0.06 mm/yr. These velocities are in relation to station VCSW (indicated on Figure 18). The magnitude of the majority of these stations is less than the average GLOBK-calculated error, which is ±0.43 mm/yr.

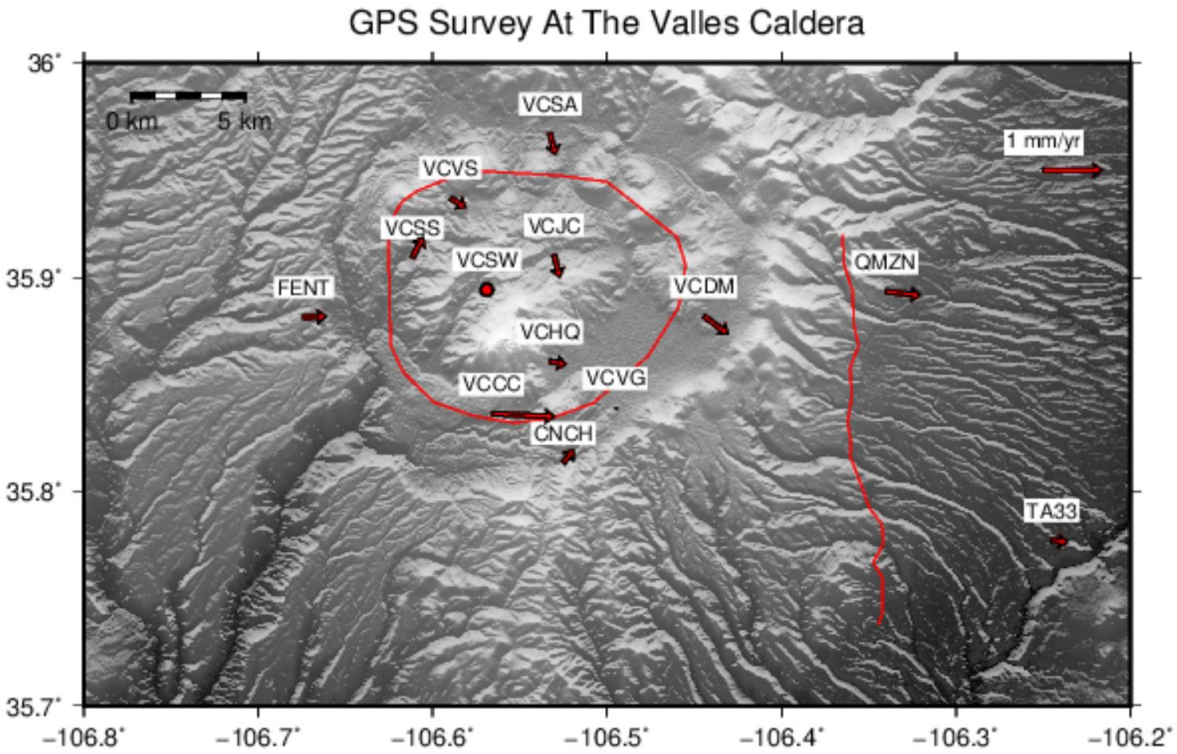

Figure A24. The 13 GPS stations processed from 2002-2022 with the GLOBK-calculated horizontal velocities indicated. The average horizontal motion is 1.13 mm/yr to the south and 0.1 mm/yr to the west. The arrow labeled “1 mm/yr” is for scale. These velocities are in relation to station VCSW (indicated on Figure 18).